



1
2 DOCTORAL THESIS

3 _____
4 Optimisation studies and background
5 estimation in searches for the supersymmetric
6 partner of the top quark in all-hadronic final
7 states with the ATLAS Detector at the LHC

8 _____
9 A thesis submitted in fulfillment of the requirements
10 for the degree of Doctor of Philosophy

11 in the
12 Experimental Particle Physics Research Group
13 School of Mathematical and Physical Sciences

14 Author: *Author:* *Supervisor:*
15 Fabrizio MIANO Dr. Fabrizio SALVATORE

15 22nd November 2017

Dedicated to my family.

*Have no fear for atomic energy
'cause none of them can stop the
time*

17

Robert Nesta Marley

18

Acknowledgments

- 19 Thanks to every single thing that went wrong. It made me stronger.

Declaration

21 I, Fabrizio MIANO, hereby declare that this thesis, titled, "Optimisation studies and back-
22 ground estimation in searches for the supersymmetric partner of the top quark in all-
23 hadronic final states with the ATLAS Detector at the LHC" has not been and will not be,
24 submitted in whole or in part to another University for the award of any other degree.

25 *Brighton, 22nd November 2017*

University of Sussex
School of Mathematical and Physical Sciences
Experimental Particle Physics Research Group

Doctoral Thesis

31
32 Optimisation studies and background estimation in searches for
33 the supersymmetric partner of the top quark in all-hadronic final
34 states with the ATLAS Detector at the LHC

by Fabrizio Miano

Abstract

38 This thesis presents searches for supersymmetry in $\sqrt{s} = 13$ TeV proton-proton collisions
39 at the LHC using data collected by the ATLAS detector in 2015, 2016 and 2017. Events
40 with 4 or more jets and missing transverse energy were selected. Kinematic variables were
41 investigated and optimisations were performed to increase the sensitivity to supersym-
42 metric signals. Standard Model backgrounds were estimated by means of Monte Carlo
43 simulations and data-driven techniques. Before analysing the data in the blinded signal
44 regions the agreement between data and background predictions and the extrapolations
45 from control and validation regions to signal regions were validated. The analysis yiel-
46 ded no significant excess in any of the analyses performed. Therefore limits were set and
47 the results were interpreted as lower bounds on the masses of supersymmetric particles
48 in various scenarios and models.

⁴⁹ Contents

⁵⁰	Introduction	1
⁵¹	1 The Standard Model of particle physics and Supersymmetry	2
⁵²	1.1 The Standard Model	2
⁵³	1.1.1 Electroweak Symmetry Breaking and the Higgs mechanism	6
⁵⁴	1.1.2 Limitations of the Standard Model	9
⁵⁵	1.2 Supersymmetry	11
⁵⁶	1.2.1 Why SUSY?	11
⁵⁷	1.2.2 Minimal Supersymmetric Standard Model	12
⁵⁸	1.2.3 Phenomenology of Supersymmetry	15
⁵⁹	2 The ATLAS Experiment at the LHC	20
⁶⁰	2.1 The LHC	20
⁶¹	2.2 The ATLAS Detector	23
⁶²	2.2.1 The Magnet System	24
⁶³	2.2.2 The Inner Detector	25
⁶⁴	2.2.3 The Calorimeters	28
⁶⁵	2.2.4 The Muon Spectrometer	29
⁶⁶	2.3 The ATLAS Trigger System	30
⁶⁷	2.3.1 Level 1 Trigger	32
⁶⁸	2.3.2 High-Level Trigger	32
⁶⁹	3 The ATLAS Trigger System	33
⁷⁰	3.1 What is the Trigger needed for?	33
⁷¹	3.2 The tracking	34
⁷²	3.3 Performance of HLT	34
⁷³	3.3.1 Electrons	34
⁷⁴	3.3.2 Muons	34

75	3.3.3 <i>b</i> -jets	34
76	4 Event Simulation and Reconstruction	35
77	4.1 Event Simulation	35
78	4.1.1 Event Generation	35
79	4.1.2 Detector Simulation	35
80	4.2 Object Reconstruction	35
81	4.2.1 Tracks and vertices	36
82	4.2.2 Electrons	36
83	4.2.3 Muons	36
84	4.2.4 Jets	36
85	4.2.5 Missing Transverse Energy	36
86	4.2.6 Overlap Removal	36
87	5 Stop searches in final states with jets and missing transverse energy	37
88	6 Results and Statistical Interpretations	38
89	Appendix A	39
90	Bibliography	40

91 List of Tables

92	1.1 Forces and mediators described by the SM	5
93	1.2 SUSY particles in the MSSM	15
94	1.3 Parameters in the pMSSM.	17

List of Figures

<p>95 List of Figures</p> <p>96 1.1 The elementary particles of the Standard Model. From the outermost to the 97 innermost; fermions (quarks, top-half wheel, leptons, bottom-half wheel), 98 vector bosons, and the Higgs boson.</p> <p>99 1.2 The Higgs potential in the complex plane.</p> <p>100 1.3 Summary of several Standard Model total production cross-section mea- 101 surements, corrected for leptonic branching fractions, compared to the cor- 102 responding theoretical expectations. All theoretical expectations were cal- 103 culated at NLO or higher. The luminosity used for each measurement is 104 indicated close to the data point. Uncertainties for the theoretical predic- 105 tions are quoted from the original ATLAS papers. They were not always 106 evaluated using the same prescriptions for PDFs and scales. Not all mea- 107 surements are statistically significant yet [1].</p> <p>108 1.4 The inverse couplings of electromagnetic (dashed blue), weak (dashed red) 109 and strong (solid green) interactions with the SM (left) and a supersymmet- 110 ric model (right). In the SM the three lines do not meet at one point, but 111 with the introduction of supersymmetry, and assuming that the supersym- 112 metric particles are not heavier than about 1 TeV, they do meet. This is an 113 indication that supersymmetry could be discovered at the LHC.</p> <p>114 1.5 NLO+NLL production cross-sections as a function of mass at $\sqrt{s} = 13\text{TeV}$ [2]</p> <p>115 1.6 Illustration of stop decay modes in the $(m_{\tilde{t}_1}, m_{\tilde{\chi}_1^0})$ mass place where the $\tilde{\chi}_1^0$ is 116 assumed to be the lightest supersymmetric particle. The dashed blue lines 117 indicate thresholds separating regions where different processes dominate.</p> <p>118 1.7 Diagrams of the decay topologies of the signal models considered in this 119 work. The term “soft” refers to decay products that have transverse mo- 120 mента below the detector thresholds.</p>	<p style="text-align: right;">3</p> <p style="text-align: right;">8</p> <p style="text-align: right;">9</p> <p style="text-align: right;">12</p> <p style="text-align: right;">18</p> <p style="text-align: right;">19</p> <p style="text-align: right;">19</p>
--	---

121	2.1 CERN Accelerator complex. The LHC is the last ring (dark grey line). Smaller machines are used for early-stage acceleration and also to provide beams for other experiments [3].	22
124	2.2 Cut-away view of the ATLAS detector. The dimensions of the detector are 25 m in height and 44 m in length. The overall weight of the detector is approximately 7000 tonnes [3].	23
127	2.3 The ATLAS magnet system.	25
128	2.4 The ATLAS Inner Detector	26
129	2.5 A computer generated image of the full calorimeter.	28
130	2.6 Cut-away view of the ATLAS muon system [4].	30
131	2.7 The ATLAS TDAQ system. L1Topo and FTK were being commissioned during 2015 and not used for the results shown in this thesis [5].	31
132		

¹³³ Introduction

¹³⁴ Last thing to write

¹³⁵ **1** | ¹³⁶ **The Standard Model of particle
physics and Supersymmetry**

¹³⁷

A theory is something nobody believes, except the person who made it. An experiment is something everybody believes, except the person who made it.

Albert Einstein

¹³⁸ In this chapter, an overview of the Standard Model of particle physics will be presented in Section 1.1 together with its limitations in Section 1.1.2. After having discussed the ¹³⁹ reasons behind the need of an extension, which theoretical physicists have been trying to ¹⁴⁰ provide for the last decades, one of the most popular, Supersymmetry, will be discussed ¹⁴¹ in Section 1.2. Here, an overview of the theory together with the motivations behind its ¹⁴² success, will be presented in Section 1.2.1, followed by the description of the Minimal ¹⁴³ Supersymmetric Standard Model (MSSM) in Section 1.2.2, and finally, the phenomenology ¹⁴⁴ of Supersymmetry, with particular attention on third-generation Supersymmetry, as ¹⁴⁵ it is the most relevant theoretical support to the analyses presented in this work, will be ¹⁴⁶ discussed in Section 1.2.3. ¹⁴⁷

¹⁴⁸ **1.1 The Standard Model**

¹⁴⁹ The SM is an effective theory that aims to provide a general description of fundamental ¹⁵⁰ particles and the phenomena we see in nature, i. e. the way they interact. Unfortunately, ¹⁵¹ our understanding of nature is still limited due to some opened question the SM is not ¹⁵² able to answer to.

¹⁵³ The 20th century can be considered a quantum revolution. Several experiments led to ¹⁵⁴ discoveries which were found to be, together with the formalised theory, a solid base of

the Standard Model of particle physics and our description of nature. Several particles were first predicted and then experimentally observed e. g. the W and the Z bosons, the τ lepton, [6], and more recently the Higgs boson at the LHC discovered by ATLAS [7] and CMS [8].

The SM lays on a Quantum Field Theory (QFT) where particles are treated like field excitations. It can describe three of the four fundamental forces; weak, electromagnetic, and strong, but not gravity.

The most general classification of the elementary particles within the SM can be made by means of spin. Fermions (leptons and quarks), usually referred to as matter, which have half-integer spin values, and bosons, usually referred to as information carriers, which have integer-spin values. A noteworthy subset of bosons is formed by the Spin-1 bosons, also known as gauge bosons. These can be considered mediators of the forces. Figure 1.1 displays the elementary particles of the Standard Model known as of today.

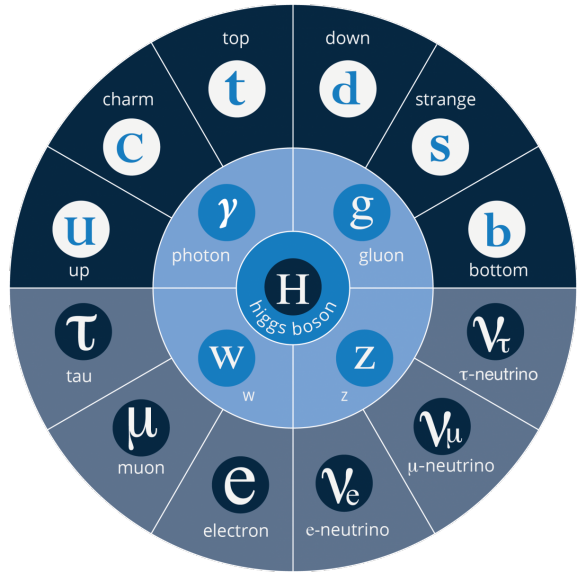


Figure 1.1: The elementary particles of the Standard Model. From the outermost to the innermost; fermions (quarks, top-half wheel, leptons, bottom-half wheel), vector bosons, and the Higgs boson.

177 Fermions

Six quarks and six leptons belong to the fermions family. In particular, fermions can be grouped into three generations. Each generation contains four particles; one up- and one down-type quark, one charged lepton and one neutral lepton. The masses of the charged leptons and quarks increase with the generation. The six quarks of the SM can be grouped into three doublets;

$$\begin{pmatrix} u \\ d \end{pmatrix}, \quad \begin{pmatrix} c \\ s \end{pmatrix}, \quad \begin{pmatrix} t \\ b \end{pmatrix}$$

The up-type quarks (*up*, *charm*, *top*) have charge $+\frac{2}{3}e$ and the down-type quarks (*down*, *strange*, *beauty/bottom*) have charge $-\frac{1}{3}e$, where e is the electron charge. Quarks also have

¹⁸⁵ another quantum number that can be seen as the analogue of the electric charge; the col-
¹⁸⁶ our charge. This can exist in three different states; *red*, *green* and *blue*. Moreover, as a con-
¹⁸⁷ sequence of *confinement*, which will be discussed later on in this section, quarks cannot
¹⁸⁸ exist as free particles. They rather group to form hadronic matter, also known as *had-*
¹⁸⁹ *rons*. There are two kinds of hadrons; mesons and baryons. Mesons are quark-antiquark
¹⁹⁰ systems, e.g. the pion, and baryons are three-quark system, e.g. protons and neutrons.
¹⁹¹ Quarks and anti-quarks have a baryon number of $\frac{1}{3}$ and $-\frac{1}{3}$, respectively.

¹⁹² There are six leptons and they can be classified in charged leptons (electron e^- , muon
¹⁹³ μ^- , tau τ^-) and neutral leptons (electron neutrino ν_e , muon neutrino ν_μ , tau neutrino ν_τ).

$$\begin{pmatrix} \nu_e \\ e^- \end{pmatrix}, \quad \begin{pmatrix} \nu_\mu \\ \mu^- \end{pmatrix}, \quad \begin{pmatrix} \nu_\tau \\ \tau^- \end{pmatrix}$$

¹⁹⁴ Each lepton has a characteristic quantum number, called lepton number (L). Negatively
¹⁹⁵ (positively) charged leptons have $L = -1$ ($L = 1$) and neutral leptons have $L = 0$. The
¹⁹⁶ lepton number is conserved in all the interactions.

¹⁹⁷ Forces of Nature

¹⁹⁸ Forces in the SM are described by gauge theories, where the interactions is mediated by
¹⁹⁹ a vector gauge boson.

²⁰⁰ The electromagnetic force is described by Quantum ElectroDynamics (QED) and, as
²⁰¹ its mediator is the photon (γ) which couples to charged particles, it only affects charged
²⁰² leptons and quarks, not neutrinos which are instead affected by the weak force, mediated
²⁰³ by the W^\pm and Z^0 bosons.

²⁰⁴ The weak interaction is associated with handedness (the projection of a particle spin
²⁰⁵ onto its direction of motion). Both leptons and quarks have left- and right-handed com-
²⁰⁶ ponents. However, only the left-handed (right-handed) component for neutrinos (anti-
²⁰⁷ neutrinos) has been observed. This means that nature prefers to produce left-handed
²⁰⁸ neutrinos and right-handed anti-neutrinos, which is the so-called *parity violation*.

²⁰⁹ The strong interaction, mediated by the gluon, electrically neutral and massless, is
²¹⁰ described by Quantum ChromoDynamics (QCD). Its coupling increases with increasing
²¹¹ distance and is smaller at short range. Moreover, due to gluon self interactions, which
²¹² will be discussed in the next paragraph, two different phenomena arise;

- ²¹³ • *confinement*: quarks or gluons cannot be observed as free particles, but only col-
²¹⁴ ourless “singlet” states can be observed as “jets”, namely collimated cone-shaped

²¹⁵ sprays of hadrons;

- ²¹⁶ • *asymptotic freedom*: interactions between quarks and gluons become weaker as the energy scale increases and the corresponding length scale decreases

²¹⁸ Table 1.1 summarises the forces described in the SM and the main characteristics of
²¹⁹ the mediators. The gravitational force is believed to be mediated by the graviton, but as
²²⁰ already mentioned, since it is not included in the SM, it will not be further discussed.

Table 1.1: Forces and mediators described by the SM

Force	Name	Symbol	Mass [GeV]	Charge
Electromagnetic	Photon	γ	0	0
Weak	W	W^\pm	80.398	$\pm e$
	Z	Z^0	91.188	0
Strong	Gluon	g	0	0

²²¹ Symmetries and Gauge Groups

²²² In 1915, the German mathematician and theoretical physicist Emmy Noether (23 March
²²³ 1882 – 14 April 1935) proved that every differentiable symmetry of the action - defined
²²⁴ as the integral over space of a Lagrangian density function - of a physical system has a
²²⁵ corresponding conservation law. More generally, a symmetry is a property of a physical
²²⁶ system and under certain transformations this property is preserved.

²²⁷ A gauge theory in QFT, is a theory in which the Lagrangian is invariant under a con-
²²⁸ tinuous group of local transformation. Group theory was adopted to describe the sym-
²²⁹ metries conserved in the SM. The gauge group of the SM is the *Lie Group* which contains
²³⁰ all the transformations between possible gauges. The Lie algebra of group generators is
²³¹ associated to any Lie group and for each group generator there emerges a corresponding
²³² field, called the gauge field, and the quanta of such fields are called *gauge bosons*.

²³³ The three SM interactions can therefore be mathematically described by the following:

$$U(1)_Y \otimes SU(2)_L \otimes SU(3)_C \quad (1.1)$$

²³⁴ Here, Y is the weak hypercharge, used to estimate the correlation between the electric
²³⁵ charge (Q) and the third component of the weak isospin (I_3) via the relation $Q = I_3 + Y/2$,
²³⁶ where I_3 can either be $\pm 1/2$ or 0 for left-handed and right-handed particles, respectively;
²³⁷ C the colour charge and L the left-handedness.

²³⁸ As of today, three of the four known forces of nature can be described using group
²³⁹ theory.

²⁴⁰ QED is an Abelian gauge theory described by the symmetry group $U(1)$. The electro-
²⁴¹ magnetic four-potential is its gauge field and the photon its gauge boson [9]. The interac-
²⁴² tions between charged fermions occurs by the exchange of a massless photon.

²⁴³ The weak interaction is described by the non-Abelian gauge group $SU(2)$. The $SU(2)$
²⁴⁴ generators are the massless gauge bosons $W_\mu^{\alpha=1,\dots,3}$ and, as mentioned earlier on in this
²⁴⁵ chapter, they violate the parity by acting only on left-handed particles. As a consequence
²⁴⁶ of non-Abelianity, $SU(2)$ gauge bosons can self-interact as the generator commutators
²⁴⁷ are non-vanishing. Additionally, quarks can also interact through weak interaction as
²⁴⁸ mixtures of SM eigenstates as described by the CKM matrix [10].

²⁴⁹ Finally, the strong interaction, described by the symmetry group $SU(3)$, has eight
²⁵⁰ massless gauge bosons, the gluons, $G_\mu^{\alpha=1,\dots,8}$ which can be exchanged between quarks
²⁵¹ and can also self-interact.

²⁵² 1.1.1 Electroweak Symmetry Breaking and the Higgs mechanism

²⁵³ In 1979 Sheldon Glashow, Abdus Salam, and Steven Weinberg were awarded the Nobel
²⁵⁴ Prize in Physics for their contributions to the so-called electroweak unification. In the
²⁵⁵ mathematical description of the SM in 1.1, the electroweak interaction is described by
²⁵⁶ $U(1)_Y \otimes SU(2)_L$.

²⁵⁷ The four electroweak physical bosons W^\pm , Z and γ are related to the four unphysical
²⁵⁸ gauge bosons $W_\mu^{\alpha=1,\dots,3}$ and B_μ . In particular, to obtain the physical bosons the gauge
²⁵⁹ bosons have to mix as follows;

$$\begin{pmatrix} A_\mu \\ Z_\mu \end{pmatrix} = \begin{pmatrix} \cos \theta_W & \sin \theta_W \\ -\sin \theta_W & \cos \theta_W \end{pmatrix} \begin{pmatrix} B_\mu \\ W_\mu^3 \end{pmatrix} \quad (1.2)$$

²⁶⁰ Here, θ_W is the so-called *Weinberg angle* which is the angle by which spontaneous sym-
²⁶¹ metry breaking rotates the original gauge bosons W_μ^3 and B_μ into the physical Z and γ .
²⁶² A_μ and Z_μ represent the photon and the Z boson, respectively. The θ_W angle can be ex-
²⁶³ perimentally determined in terms of the coupling strengths, of the $B_\mu(g_1)$ and the $W_\mu^\alpha(g_2)$
²⁶⁴ to the fermions, using the relation $\tan \theta_W = g_1/g_2$. The field mixing of gauge bosons that
²⁶⁵ gives birth to the physical ones can be mathematically expressed by the following:

$$A_\mu = W_\mu^3 \sin \theta_W + B_\mu \cos \theta_W \quad (1.3)$$

266

$$Z_\mu = W_\mu^3 \cos \theta_W - B_\mu \sin \theta_W \quad (1.4)$$

267 and the two charged W bosons are defined as;

$$W_\mu^\pm = \frac{1}{\sqrt{2}} (W_\mu^1 \mp i W_\mu^2) \quad (1.5)$$

268 The mass terms for both gauge bosons and fermionic fields are forbidden by the elec-
 269 troweak gauge as they are not invariant under gauge transformations. Nonetheless, it was
 270 experimentally proven that W and Z bosons are massive [9], therefore in order for the SM
 271 assumption to hold, the electroweak symmetry must be broken.

272 The SM Lagrangian can be written as the sum of the various Lagrangians describing
 273 the three interactions and the masses of the elementary particles as follows:

$$\mathcal{L}_{\text{SM}} = \mathcal{L}_{\text{EWK}} + \mathcal{L}_{\text{QCD}} + \mathcal{L}_{\text{Mass}} \quad (1.6)$$

274 In order for the SM Lagrangian to remain a renormalisable theory, the mass terms ($\mathcal{L}_{\text{Mass}}$)
 275 cannot be inserted by hand. A mechanism, that can preserve the gauge symmetry in the
 276 SM and can solve the inconsistency arisen from the mass difference between the gauge
 277 bosons and the physical ones, is needed. A British theoretical physicist, Peter Higgs (29
 278 May 1929, Newcastle upon Tyne, UK), came up with a brilliant solution for which he was
 279 awarded the Nobel Prize in Physics in 2013. Higgs proposed that broken symmetry in
 280 the electroweak theory could explain the origin of masses of elementary particles, and
 281 in particular of W and Z bosons. It was around 1960's when the Higgs mechanism was
 282 about to be given birth. The mechanism introduces a scalar field, known as the Higgs
 283 field, thought to couple to both massive fermions and bosons. The $SU(2)$ doublet is then
 284 introduced in the SM;

$$\phi = \begin{pmatrix} \phi^+ \\ \phi^0 \end{pmatrix} \quad (1.7)$$

285 with ϕ^+ and ϕ^0 generic complex fields:

$$\phi^+ = \frac{\phi_1 + i\phi_2}{\sqrt{2}}, \quad \phi^0 = \frac{\phi_3 + i\phi_4}{\sqrt{2}} \quad (1.8)$$

286 Consider a Lagrangian of the form:

$$\mathcal{L}_{\text{Higgs}} = (\partial_\mu \phi)^* (\partial^\mu \phi) - V(\phi) \quad (1.9)$$

²⁸⁷ Renormalizability and $SU(2)_L \otimes U(1)_Y$ invariance require the Higgs potential to be of the
²⁸⁸ following form:

$$V(\phi) = \mu^2 \phi^\dagger \phi + \lambda (\phi^\dagger \phi)^2 \quad (1.10)$$

²⁸⁹ The Lagrangian in Eq. 1.9 is the Higgs Lagrangian if ϕ is chosen to be the following:

$$\phi = \begin{pmatrix} \phi^+ \\ \phi^0 \end{pmatrix} = \begin{pmatrix} G^+ \\ \frac{1}{\sqrt{2}}(v + H + iG^0) \end{pmatrix}$$

²⁹⁰ Here, the complex scalar field G^\pm and the real scalar field G^0 correspond to Goldstone
²⁹¹ bosons, and the real scalar field H is the SM Higgs boson field [11]. These massless scalars
²⁹² are absorbed due to the gauge transformations by the electroweak gauge bosons of the SM:

$$\phi = \begin{pmatrix} \phi^+ \\ \phi^0 \end{pmatrix} = \begin{pmatrix} 0 \\ \frac{1}{\sqrt{2}}(v + H) \end{pmatrix} \quad (1.11)$$

²⁹³ The Higgs potential in Eq. 1.10 is displayed in Fig. 1.2 if λ and μ are chosen to be real.
²⁹⁴ Such potential has a non-zero ground state, v , also known as *vacuum expectation value*
²⁹⁵ (VEV):

$$\phi_0 = \begin{pmatrix} 0 \\ \frac{1}{\sqrt{2}}v \end{pmatrix} \quad (1.12)$$

²⁹⁶ Such representation remains invariant under $U(1)$ allowing electric charge conservation.
²⁹⁷ However, the SM gauge symmetry 1.1 is broken into $SU(2)_L \otimes U(1)_Y$.

²⁹⁸

In summary, to generate particle masses

²⁹⁹

gauge symmetry must be broken. However, in order for the theory to remain renormalisable, the global Lagrangian symmetry must be preserved. This can be solved introducing the concept of *spontaneous symmetry breaking* (SSB): a mechanism that allows a symmetric Lagrangian, but not a symmetric VEV. In particular,

³⁰⁰

³⁰¹

³⁰²

³⁰³

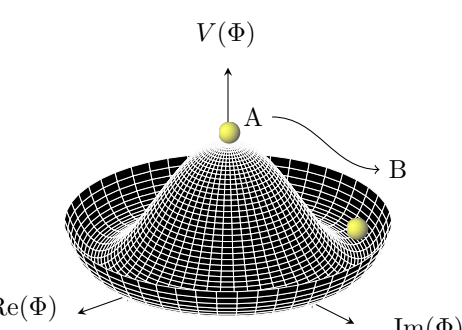
³⁰⁴

³⁰⁵

³⁰⁶

³⁰⁷ Figure 1.2: The Higgs potential in the complex plane.

³⁰⁸



given a Lagrangian invariant under a certain transformation, T_X , and a generic set

of states, that transform under T_X as the elements of a multiplet, the symmetry is spontaneously broken if one of those states is arbitrarily chosen as the ground state of the system. The interaction of the Higgs field with the $SU(2) \otimes U(1)$ gauge fields, $W_\mu^{\alpha=1,2,3}$, result in the three gauge bosons fields acquiring mass whilst the B_μ field remains massless.

1.1.2 Limitations of the Standard Model

During Run 1 and 2 of the LHC, the SM has been extensively validated, as shown in Fig. 1.3: the agreement, between the measured production cross-section of various SM processes and the SM predictions, looks very good. However, the reasons behind the mass difference between the three generations of fermions are still not explained by the SM, since masses are treated as free parameters in the theory. In addition, there are some fundamental questions that have still no answer and they will be briefly discussed this section.

Standard Model Total Production Cross Section Measurements Status: July 2017

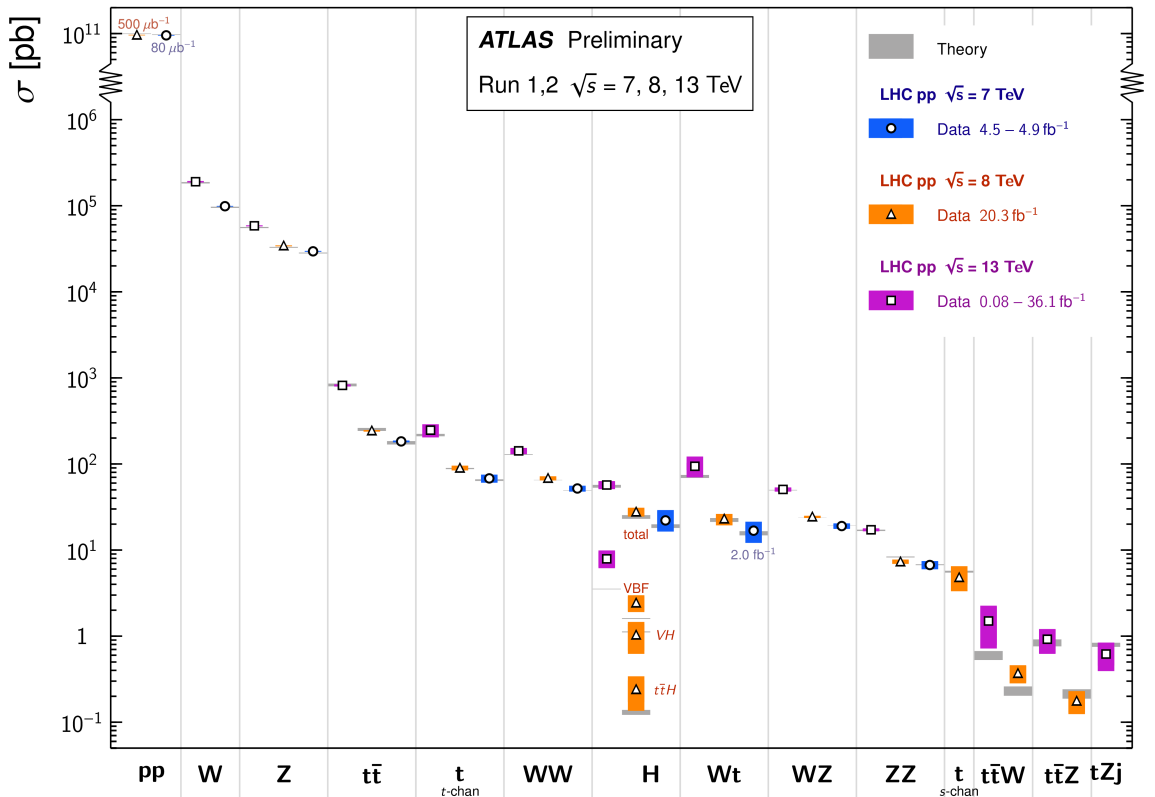


Figure 1.3: Summary of several Standard Model total production cross-section measurements, corrected for leptonic branching fractions, compared to the corresponding theoretical expectations. All theoretical expectations were calculated at NLO or higher. The luminosity used for each measurement is indicated close to the data point. Uncertainties for the theoretical predictions are quoted from the original ATLAS papers. They were not always evaluated using the same prescriptions for PDFs and scales. Not all measurements are statistically significant yet [1].

321 Hierarchy Problem

322 Due to the coupling of the Higgs field to the fermionic fields the one-loop corrections to
323 the Higgs mass receive several contributions. In particular:

$$\Delta m_H^2 = -\frac{|\lambda_f|^2}{8\pi^2} \Lambda_{\text{UV}}^2 + \dots \quad (1.13)$$

324 where, λ_f is the coupling constant to the fermionic field; Δm_H^2 is the difference between
325 the observed Higgs mass m_H^2 and the bare mass, m_H^0 (Lagrangian parameter); Λ_{UV} is
326 the ultraviolet momentum cut-off, selected to be at the Planck scale ($\sim 2 \cdot 10^{18}$ GeV), at
327 which a QFT description of gravity is believed to become possible. The correction to the
328 Higgs mass then, will be around 30 orders of magnitude larger than Higgs mass itself,
329 in opposition to what has been measured. This difference just mentioned, between the
330 electroweak scale and the Planck scale arisen from the quantum corrections to the Higgs
331 mass, is the so-called Hierarchy Problem [12].

332 Neutrino Masses

333 The Super-Kamiokande Collaboration first, in 1998 [13], and SNO Collaboration later, in
334 2001 [14], have provided measurements of the neutrino flux from solar and atmospheric
335 sources. The Nobel Prize in Physics 2015 was awarded jointly to Takaaki Kajita and Arthur
336 B. McDonald “for the discovery of neutrino oscillations, which shows that neutrinos have
337 mass” [15]. Such feature contradicts the absence of a mechanism for mass generation for
338 the neutrinos.

339 Dark Matter

340 Although dark matter (DM) has never been directly observed, its existence is inferred from
341 its gravitational effects. For example, looking at galaxies rotation, it was observed that the
342 rotation speed was higher than expected, given the amount of visible matter. Two differ-
343 ent reasoning arose during the last century to justify such effect: there is either matter that
344 cannot be seen by us (in terms of visible light), which contributes to the galactic mass, or
345 the general relativity works differently at galactic distances. The former is believed to
346 be the most likely and it implies the existence of new particles which do not interact via
347 electromagnetic interaction, the so-called Weakly Interacting Massive Particles (WIMPs).

348 1.2 Supersymmetry

349 Supersymmetry, also known as SUSY, introduces a space-time symmetry that relates bo-
 350 sons to fermions and vice-versa, via a transformation of the form of:

$$Q |\text{fermion}\rangle = |\text{boson}\rangle, \quad Q |\text{boson}\rangle = |\text{fermion}\rangle \quad (1.14)$$

351 For each SM particle there exists a supersymmetric partner, generally called *sparticle* (where
 352 the s stands for “scalar”), with a spin difference of $\Delta s = 1/2$. Each pair of partners is ar-
 353 ranged in a so-called *supermultiplet*. The two components have same masses and quantum
 354 numbers, but different spin. *Sleptons* and *squarks* gauge mechanism is the same as their SM
 355 equivalent, namely for example, the superpartners of the left-handed SM fermion com-
 356 ponents couple weakly, but the superpartners of the right-handed SM fermion com-
 357 ents do not. Furthermore, gauge supermultiplets contain a vector boson and two spin-
 358 $\frac{1}{2}$ fermions. Spin-1 bosons are arranged in gauge multiplets, and their superpartners,
 359 referred to as *gauginos*, are spin- $\frac{1}{2}$ fermions. Differently from the SM, the Spin-0 Higgs
 360 boson has two supermultiplets containing sparticles with different weak isospin values,
 361 referred to as H_u and H_d , which are required to give mass to both the up- and down-type
 362 sparticles. Higgs SUSY partners are called the *Higgsinos*.

363 As of today, SUSY particles have not been observed, resulting in the assumption that
 364 SUSY must be a broken symmetry, otherwise superpartners would have the same quantum
 365 numbers and masses as their SM equivalent. However, if sparticles were to be too heavy
 366 (close to the Planck scale), the hierarchy problem would still remain unsolved. The *soft*
 367 SUSY breaking mechanism, described in Section 1.2.2, overcomes this problem by impos-
 368 ing constraints on the masses of sparticles to a range that can be experimentally explored.

369 1.2.1 Why SUSY?

370 One of the main motivations for SUSY is the cancellation of quadratic divergences to
 371 Δm_H^2 . The introduction of SUSY particles, with a half-integer spin difference with re-
 372 spect to their SM partners, provides a solution to the hierarchy problem. The Higgs mass
 373 squared potential receives corrections from a new scalar of mass m_S of the form:

$$\Delta m_H^2 = -\frac{|\lambda_S|^2}{16\pi^2} \left[\Lambda_{\text{UV}}^2 - 2m_S^2 \ln(\Lambda_{\text{UV}}/m_S) + \dots \right] \quad (1.15)$$

374 where, λ_S is the coupling of SUSY particles to the Higgs field. This term cancels the
 375 fermionic contributions in Eq. 1.13 since the couplings are the same. The experimental

³⁷⁶ value of Higgs mass will then not need any fine tuning.

³⁷⁷ Furthermore, Fig. 1.4 shows the inverse couplings as a function of the scale for both SM
³⁷⁸ and the Minimal Supersymmetric Standard Model (MSSM), which will be soon discussed.

³⁷⁹ In the SM the three lines, representing electromagnetic (dashed blue), weak (dashed red)
³⁸⁰ and strong (solid green) interactions respectively, do not meet at one point, but with the
³⁸¹ introduction of supersymmetry, and assuming that the supersymmetric particles are not
³⁸² heavier than about 1 TeV, they do meet. This is an indication that supersymmetry could
³⁸³ be discovered at the LHC as well as another good motivation for SUSY searches given the
³⁸⁴ possible unification of the coupling constants at the Planck scale.

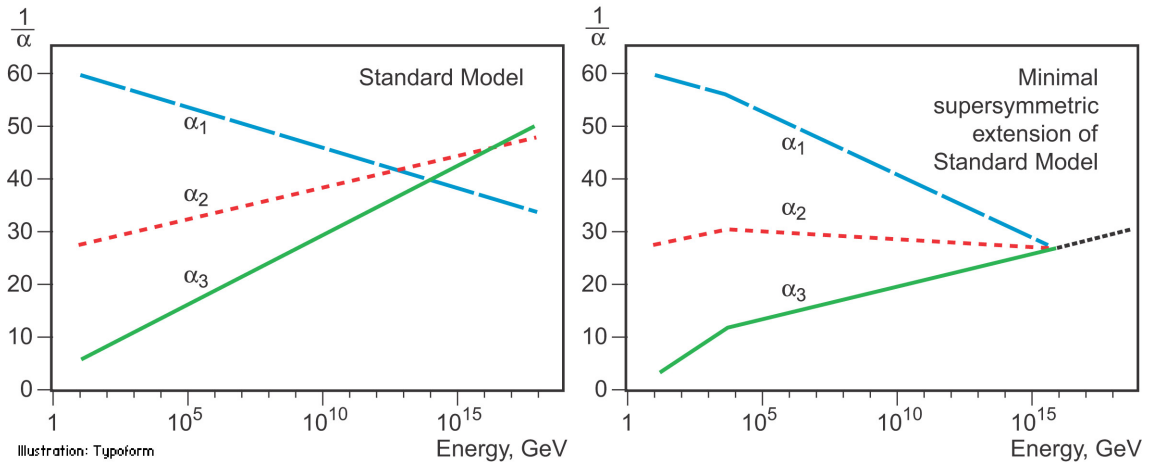


Figure 1.4: The inverse couplings of electromagnetic (dashed blue), weak (dashed red) and strong (solid green) interactions with the SM (left) and a supersymmetric model (right). In the SM the three lines do not meet at one point, but with the introduction of supersymmetry, and assuming that the supersymmetric particles are not heavier than about 1 TeV, they do meet. This is an indication that supersymmetry could be discovered at the LHC.

³⁸⁵ 1.2.2 Minimal Supersymmetric Standard Model

³⁸⁶ There does not exist a unique extension of a supersymmetric Standard Model, i. e. SUSY
³⁸⁷ is not a well-defined model but it is more a framework within which various SM exten-
³⁸⁸ sions can be derived. The Minimal Supersymmetric Standard Model (MSSM), a minimal
³⁸⁹ supersymmetric extension of the SM [16], is defined by essentially doubling up the num-
³⁹⁰ ber of particles in the SM theory in order to include all the SM particles as well as their
³⁹¹ corresponding superpartners.

392 Soft SUSY breaking

393 The mass spectrum of the SUSY particles must sit somewhere at a larger scale than the SM
394 one, as supersymmetric particles have not been discovered at the mass scale of their SM
395 partners. This gives us a hint that supersymmetry cannot be an exact symmetry, there has
396 to be an analogous to the electroweak symmetry breaking discussed in [1.1.1](#) that breaks
397 SUSY. In particular, this must be soft or spontaneous such that broken supersymmetry
398 still provides a solution to the hierarchy problem. This means that some new higher-
399 energy-scale particles and interactions have to be added to the MSSM, but it also means
400 that terms, containing only masses and couplings, with positive mass dimension, gauge
401 invariant and violating SUSY, have to be added to the Lagrangian;

$$\mathcal{L}_{\text{MSSM}} = \mathcal{L}_{\text{SUSY}} + \mathcal{L}_{\text{soft}} \quad (1.16)$$

402 Here, $\mathcal{L}_{\text{SUSY}}$ contains the original SUSY invariant interaction and $\mathcal{L}_{\text{soft}}$ contains all the
403 additional terms. A set of around 100 parameters - depending on the method - are then
404 introduced into the theory.

405 A large amount of theoretical effort has been spent trying to understand the mech-
406 anism for soft SUSY breaking in order to produce the desired superpartner masses and
407 interactions properties. Among these three most studied mechanisms are;

- 408** • gravity-mediated supersymmetry breaking, also known as mSUGRA (minimal su-
409 pergravity), which communicates supersymmetry breaking to the supersymmetric
410 Standard Model through gravitational interactions [[17](#)];
- 411** • gauge-mediated supersymmetry breaking (GMSB) which communicates supersym-
412 metry breaking to the supersymmetric Standard Model through the Standard Model's
413 gauge interactions [[18](#)];
- 414** • anomaly-mediated supersymmetry breaking (AMSB), a special type of gravity-mediated
415 supersymmetry breaking, that communicates supersymmetry breaking to the su-
416 persymmetric Standard Model through the conformal anomaly [[19, 20](#)]

417 However, such models will not be discussed any further.

418 MSSM mass spectrum

419 As per the SM gauge bosons, the gaugino masses are affected by electroweak symmetry
420 breaking. The new mass terms, introduced in the $\mathcal{L}_{\text{soft}}$, mix to form the mass eigenstates

⁴²¹ of the sparticles. The neutral Winos, \tilde{W}^0 , Binos, \tilde{B}^0 and higgsinos \tilde{H}^0 mix to form the four
⁴²² *neutralinos* $\tilde{\chi}_i^0$ ($i = 1, 2, 3, 4$) as it follows;

$$\begin{pmatrix} \tilde{\chi}_1^0 \\ \tilde{\chi}_2^0 \\ \tilde{\chi}_3^0 \\ \tilde{\chi}_4^0 \end{pmatrix} = \begin{pmatrix} M_1 & 0 & -c_\beta s_W m_Z & c_W s_\beta m_Z \\ 0 & M_2 & c_\beta c_W m_Z & -c_W s_\beta m_Z \\ -c_\beta s_W m_Z & c_\beta s_W m_Z & 0 & -\mu \\ s_\beta c_W m_Z & -s_\beta c_W m_Z & -\mu & 0 \end{pmatrix} \begin{pmatrix} \tilde{B}^0 \\ \tilde{W}^0 \\ \tilde{H}_u^0 \\ \tilde{H}_d^0 \end{pmatrix} \quad (1.17)$$

⁴²³ Here, $c_\beta = \cos \beta$, $(s_\beta) = \sin \beta$, $c_W = \cos \theta_W$ and $(s_W) = \sin \theta_W$. M_1 , M_2 are related
⁴²⁴ to gaugino masses and μ to higgsino mass, β is the ratio of the electroweak coupling
⁴²⁵ constants and θ_W is the ratio of the VEVs of the two Higgs doublet fields, and finally, m_Z
⁴²⁶ (m_W) is the mass of the Z (W) boson. The neutralino indeces are conventionally assumed
⁴²⁷ to increase with their masses. The charged winos \tilde{W}^\pm and higgsinos \tilde{H}^\pm mix to form four
⁴²⁸ *charginos*, $\tilde{\chi}_i^\pm$ ($i = 1, 2$) as it follows;

$$\begin{pmatrix} \tilde{\chi}_1^\pm \\ \tilde{\chi}_2^\pm \end{pmatrix} = \begin{pmatrix} M_2 & \sqrt{2}m_W s_\beta \\ \sqrt{2}m_W c_\beta & \mu \end{pmatrix} \begin{pmatrix} \tilde{W}^\pm \\ \tilde{H}^\pm \end{pmatrix} \quad (1.18)$$

⁴²⁹ Charginos and neutralinos, given birth by the mixing described in Eq. 1.18 and 1.17,
⁴³⁰ will be referred to as bino-like, wino-like or higgsino-like depending on their phenomenology.
⁴³¹ Gluinos do not mix as they carry colour charge.

⁴³² The Higgs sector is also affected. There are five mass eigenstates, h^0 , H^0 , A^0 , and H^\pm .
⁴³³ These, together with the other MSSM particles are listed in Table 1.2.

⁴³⁴ In the MSSM the squark sector is specified by the mass matrix in the basis $(\tilde{q}_L, \tilde{q}_R)$ with
⁴³⁵ $\tilde{q} = \tilde{t}$ or \tilde{b} [21]. Left- and right-handed squarks and sleptons do not have to have equal
⁴³⁶ mass, which means that a rotation matrix can be defined, although the mixing is assumed
⁴³⁷ to be non-zero only for the third-generation scalar partners. Stop, \tilde{t}_L , \tilde{t}_R , sbottom \tilde{b}_L , \tilde{b}_R ,
⁴³⁸ and stau, $\tilde{\tau}_L$, $\tilde{\tau}_R$ rotate into mass eigenstates, \tilde{t}_1 , \tilde{t}_2 , \tilde{b}_1 , \tilde{b}_2 , $\tilde{\tau}_1$, $\tilde{\tau}_2$, respectively, as described
⁴³⁹ in Eq. 1.19 [22].

$$\mathcal{M}_q^2 = \begin{pmatrix} m_{\tilde{q}_L}^2 & a_q m_q \\ a_q m_q & m_{\tilde{q}_R}^2 \end{pmatrix} \quad (1.19)$$

⁴⁴⁰ with

Table 1.2: SUSY particles in the MSSM

Name	Spin	Gauge Eigenstates	Mass Eigenstates
Squarks (\tilde{q})	0	$\tilde{u}_L \tilde{u}_R \tilde{d}_L \tilde{d}_R$	(same)
		$\tilde{c}_L \tilde{c}_R \tilde{s}_L \tilde{s}_R$	(same)
		$\tilde{t}_L \tilde{t}_R \tilde{b}_L \tilde{b}_R$	$\tilde{t}_1 \tilde{t}_2 \tilde{b}_1 \tilde{b}_2$
Sleptons (\tilde{l})	0	$\tilde{e}_L \tilde{e}_R \tilde{\nu}_L$	(same)
		$\tilde{\mu}_L \tilde{\mu}_R \tilde{\nu}_L$	(same)
		$\tilde{\tau}_L \tilde{\tau}_R \tilde{\nu}_{\tau}$	$\tilde{\tau}_1 \tilde{\tau}_2 \tilde{\nu}_{\tau}$
Higgs bosons	0	$H_u^0 H_d^0 H_u^+ H_d^-$	$h^0 H^0 A^0 H^{\pm}$
Neutralinos ($\tilde{\chi}_j^0$)	1/2	$\tilde{B}^0 \tilde{W}^0 \tilde{H}_u^0 \tilde{H}_d^0$	$\tilde{\chi}_1^0 \tilde{\chi}_2^0 \tilde{\chi}_3^0 \tilde{\chi}_4^0$
Charginos ($\tilde{\chi}_i^{\pm}$)	1/2	$\tilde{W}^{\pm} \tilde{H}_u^{\pm} \tilde{H}_d^{\mp}$	$\tilde{\chi}_1^{\pm} \tilde{\chi}_2^{\pm}$
Gluino	1/2	\tilde{g}	(same)
Gravitino	3/2	\tilde{G}	(same)

$$\begin{aligned}
m_{\tilde{q}_L}^2 &= M_{\tilde{Q}}^2 + m_Z^2 \cos 2\beta \left(I_3^{q_L} - e_q \sin^2 \theta_W \right) + m_q^2, \\
m_{\tilde{q}_R}^2 &= M_{\{\tilde{U}, \tilde{D}\}}^2 + m_Z^2 \cos 2\beta e_q \sin^2 \theta_W + m_q^2, \\
a_q m_q &= \begin{cases} (A_t - \mu \cot \beta) m_t, (\tilde{q} = \tilde{t}) \\ (A_b - \mu \tan \beta) m_t, (\tilde{q} = \tilde{b}) \end{cases}
\end{aligned} \tag{1.20}$$

Here, $I_3^{q_L}$ is the third component of the weak isospin and e_q the electric charge of the quark q . $M_{\{\tilde{Q}, \tilde{U}, \tilde{D}\}}$ and $A_{t,b}$ are soft SUSY-breaking parameters, μ is the higgsino mass parameter, and $\tan \beta$ is the ratio of Higgs field VEVs. By diagonalising the matrix in Eq. 1.19 one gets the mass eigenstates

$$\tilde{q}_1 = \tilde{q}_L \cos \theta_{\tilde{q}} + \tilde{q}_R \sin \theta_{\tilde{q}}$$

$$\tilde{q}_2 = -\tilde{q}_L \sin \theta_{\tilde{q}} + \tilde{q}_R \cos \theta_{\tilde{q}}$$

with the mass eigenvalues $m_{\tilde{q}_1}, m_{\tilde{q}_2}$ ($m_{\tilde{q}_1} < m_{\tilde{q}_2}$) and the mixing angle $\theta_{\tilde{q}}$ ($-\pi/2 < \theta_{\tilde{q}} \leq \pi/2$).

1.2.3 Phenomenology of Supersymmetry

As previously mentioned, the introduction of SUSY particles overcomes the problem of an unnatural fine-tuning to the Higgs mass due to its quadratic corrections, given that the stops have masses typically around 1 TeV.

450 ***R*-parity**

451 The most general MSSM can contain operators that violate baryon and/or lepton number,
 452 thus allowing proton decays. The non-observation of proton decays forbids the existence
 453 of such terms. A possibility to avoid these operators is to introduce a new discrete sym-
 454 metry named *R*-parity. The conserved quantum number is defined as;

$$P_R = (-1)^{3(B-L)+2s} \quad (1.21)$$

455 where B , L , and s are the baryon, lepton, and spin number, respectively.

456 If a certain SUSY model is *R*-parity conserving, then the SM particles have $R = 1$ and
 457 SUSY partners have $R = -1$. When *R*-parity conservation is imposed on MSSM models,
 458 the mixing between particles and sparticles cannot occur, resulting in the number of SUSY
 459 particles to be even at every interaction vertex. Furthermore, all sparticles must be pair-
 460 produced and the Lightest Supersymmetric Particle (LSP) has to be stable and can be a
 461 good Dark Matter candidate.

462 Although the SUSY searches in a *R*-parity violating (RPV) scenario have been ex-
 463 tensively investigated by the particle-physics community, in this work only *R*-parity con-
 464 serving (RPC) models, where the $\tilde{\chi}_1^0$ is assumed to be the LSP, were considered.

465 **Phenomenological MSSM (pMSSM)**

466 As mentioned in 1.2.2, once the SUSY soft breaking occurred, the unconstrained MSSM
 467 has more than 100 parameters in addition to the Standard Model ones. However, this
 468 makes the SUSY searches, e.g. finding regions, in parameter space, that are consistent
 469 with the data, rather impractical. Under the following three assumptions;

470 • no new source of CP-violation (CKM matrix is the only source)

471 • no Flavour Changing Neutral Currents

472 • first- and second-generation universality

473 the number of free parameters can be reduced down to 19. The introduction of such para-
 474 meters, summarised in Table 1.3, defines the so-called phenomenological MSSM (pMSSM).
 475 Such parameter space is still rather large and it makes pMSSM searches extremely chal-
 476 lenging and difficult to exclude. To overcome this problem *simplified models* are introduced.
 477 In other words, a certain signal process is extracted from the model and only particles
 478 contributing to a certain decay mode will be considered, e.g. $\tilde{t}_1 \rightarrow t + \tilde{\chi}_1^0$ only targets the

Table 1.3: Parameters in the pMSSM.

Parameter	Description	N. of parameters
M_1, M_2, M_3	Bino, Wino and gluino masses	3
M_A	pseudoscalar Higgs boson mass	1
μ	higgsino mass	1
$m_{\tilde{q}}, m_{\tilde{u}_R}, m_{\tilde{d}_R}$, $m_{\tilde{Q}_L}, m_{\tilde{t}}, m_{\tilde{b}}$	first- and second-generation squark masses third generation squark masses	3 3
$m_{\tilde{l}}, m_{\tilde{e}_R}$ $m_{\tilde{L}}, m_{\tilde{\tau}_R}$	first- and second-generation slepton masses third-generation slepton masses	2 2
A_t, A_b, A_τ	third-generation trilinear couplings	3
$\tan \beta$	two-higgs-doublet fields VEVs ratio	1

479 2-body decay ignoring the remaining SUSY mass spectrum. The number of parameters
480 will then boil down to 2; $m_{\tilde{t}}$ and $m_{\tilde{\chi}^0}$, allowing the reinterpretation of the results and
481 providing a powerful tool to constrain various models.

482 In this work only analyses laying their theoretical assumptions on such simplified
483 models will be presented.

484 Phenomenology of the top squark

485 Fig. 1.5 shows SUSY particles production cross-sections for squarks that do not contrib-
486 ute to gluino production diagrams and vice versa, i. e. treating squarks and gluinos as
487 *decoupled* making the cross-section of squark pair-production be the same for all famil-
488 ies. While gluinos production cross-sections are fairly large, SUSY electroweak produc-
489 tion cross-sections of neutralinos and charginos are considerably lower. Sleptons pro-
490 duction cross-section, which is not displayed, would sit just below higgsino-like char-
491 gino/neutralino production cross-section.

492 Due to the cross-section being around a factor of six smaller than $t\bar{t}$ production (when
493 $m_{\tilde{t}_1} \sim m_t$), third-generation SUSY analyses are very challenging. Furthermore, the cross-
494 section of such processes dramatically decreases with increasing $m_{\tilde{q}}$. Nonetheless, for
495 example, searches for direct \tilde{t}_1 production with $\tilde{t}_1 \rightarrow t + \tilde{\chi}_1^0$ are sensitive in a scenario
496 where $m_{\tilde{t}_1} \gg m_t + m_{\tilde{\chi}_1^0}$ as the large E_T^{miss} , from the neutralinos, provides discriminating
497 power for $t\bar{t}$ rejection.

498 There exists various decay modes of pair-produced stops, depending on the masses
499 of the decay products;

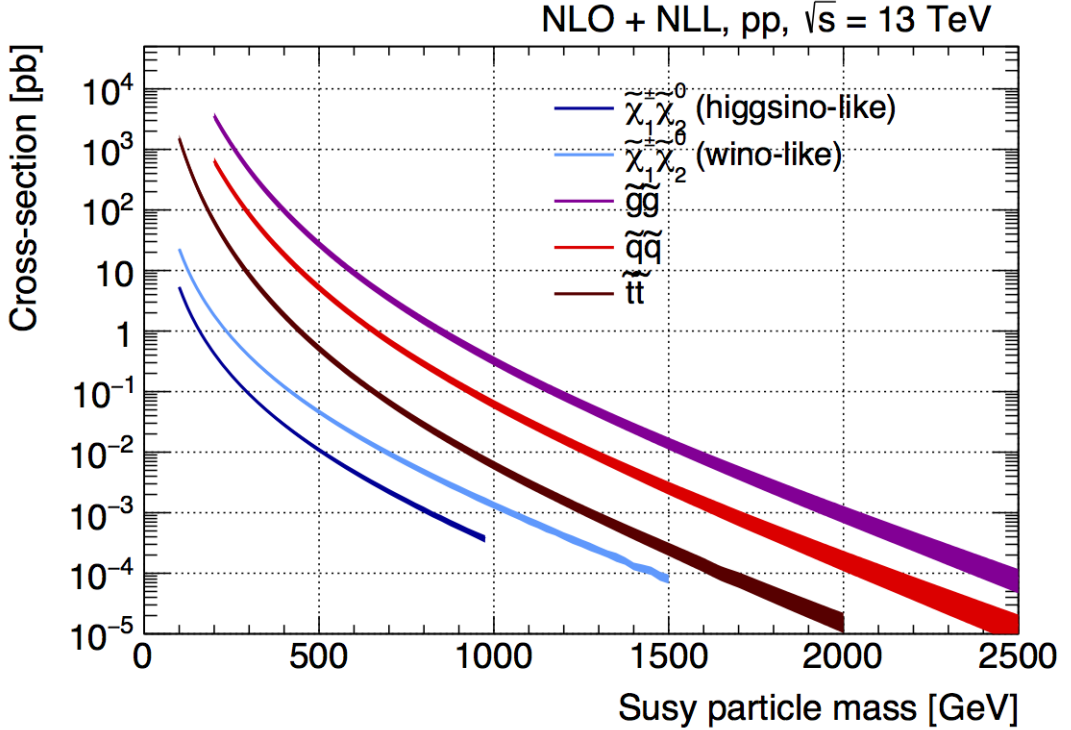


Figure 1.5: NLO+NLL production cross-sections as a function of mass at $\sqrt{s} = 13$ TeV [2]

- 500 • $\tilde{t} \rightarrow t \tilde{\chi}^0$
- 501 • $\tilde{t} \rightarrow b \tilde{\chi}^\pm \rightarrow b W \tilde{\chi}^0$ (on/off-shell W) or $\tilde{t} \rightarrow b W \tilde{\chi}^0$ (off-shell top)
- 502 • $\tilde{t} \rightarrow c \tilde{\chi}^0$
- 503 • $\tilde{t} \rightarrow b f f' \tilde{\chi}^0$

504 Figure 1.6 shows a schematic representation of the parameter space $(m_{\tilde{t}_1}, m_{\tilde{\chi}_1^0})$ and the
505 different region where each of the above-mentioned process dominates.

506 In the models considered in this work, either $\tilde{\chi}_2^0$ or $\tilde{\chi}_1^\pm$ is assumed to be the so-called
507 next lightest supersymmetric particle (NLSP). Three different decay scenarios were con-
508 sidered in this work; (a) where both top squarks decay via $\tilde{t} \rightarrow t^{(*)} \tilde{\chi}_1^0$ ¹; (b) at least one
509 of the stops decays via $\tilde{t} \rightarrow b \tilde{\chi}_1^\pm \rightarrow b W^{(*)} \tilde{\chi}_1^0$; (c) where $m_{\tilde{\chi}_2^0}$ is small enough to allow
510 one stop to decay via $\tilde{t} \rightarrow t \tilde{\chi}_2^0 \rightarrow h/Z \tilde{\chi}_1^0$. Here, h is the SM Higgs boson (125 GeV),
511 as illustrated in Figure 1.7(a)–(c), respectively. Furthermore, top squarks can also be in-
512 directly produced through the so-called gluino-mediated stop production, as shown in
513 Figure 1.7(d).

¹ The symbol (*) indicates that the decay can occur with the top quark being produced off-shell (region between the second and third dashed line in Fig. 1.6)

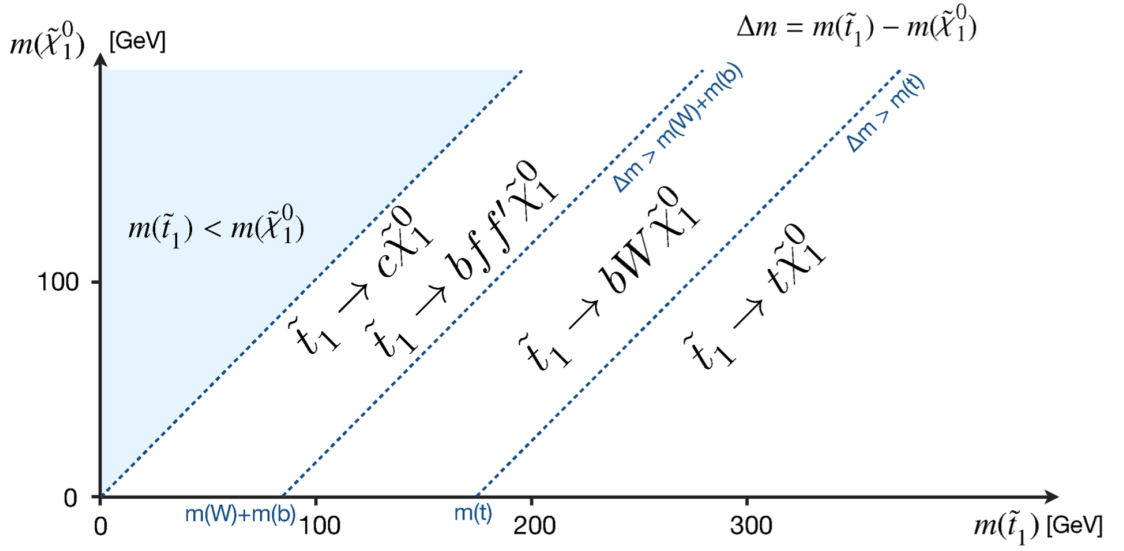


Figure 1.6: Illustration of stop decay modes in the $(m_{\tilde{t}_1}, m_{\tilde{\chi}_1^0})$ mass place where the $\tilde{\chi}_1^0$ is assumed to be the lightest supersymmetric particle. The dashed blue lines indicate thresholds separating regions where different processes dominate.

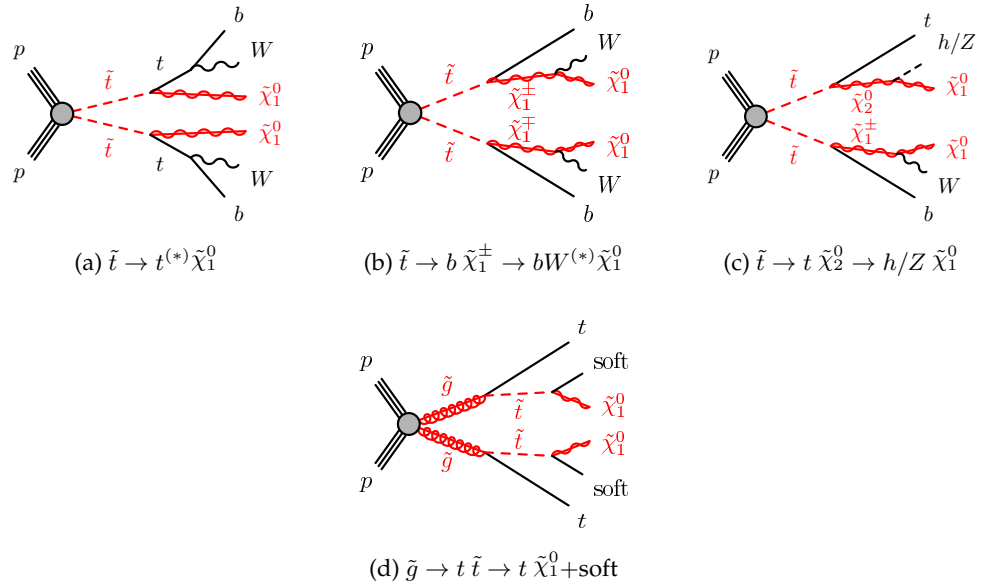


Figure 1.7: Diagrams of the decay topologies of the signal models considered in this work. The term “soft” refers to decay products that have transverse momenta below the detector thresholds.

514 **2** | **The ATLAS Experiment at the**
515 **LHC**

516

*We are rather like children, who
 must take a watch to pieces to see
 how it works*

Sir Ernest Rutherford

517 ATLAS (A Toroidal LHC ApparatuS) is one of the four main experiments (ATLAS,
518 CMS, ALICE, LHCb) taking data at a center-of-mass energy of 13 TeV using beams de-
519 livered by the Large Hadron Collider (LHC). In this chapter an overview of the LHC will
520 be given in Section 2.1, then the ATLAS detector will be described in Section 2.2, and fi-
521 nally the Trigger system, used to cleverly store the data, will be described in Section 2.3. A
522 more in-depth description of the Trigger algorithms I have been involved in will be given
523 in Chapter 3.

524 **2.1 The LHC**

525 As of today, the LHC is the world's largest and most powerful particle accelerator. It was
526 designed to help answer some of the fundamental open questions in particle physics by
527 colliding protons at an unprecedented energy and luminosity. It is located at the European
528 Organisation for Nuclear Research (CERN), in the Geneva area, at a depth ranging from
529 50 to 175 metres underground. It consists of a 27-kilometre ring made of superconducting
530 magnets, and inside it two high-energy particle beams travel in opposite directions and
531 in separate beam pipes.

532 The beams are guided around the ring by a strong magnetic field generated by coils -
533 made of special electric cables - that can operate in a superconducting regime. 1232 super-
534 conducting dipole and 392 quadrupole magnets, with an average magnetic field of 8.3 T,

535 are employed and kept at a temperature below 1.7 K, in order to preserve their supercon-
 536 ducting properties. The formers are used to bend the beams and the latters to keep them
 537 focused while they get accelerated.

538 The collider first went live on September 2008 even though, due to a magnet quench
 539 incident that damaged over 50 superconducting magnets, it has been operational since
 540 November 2009 when low-energy beams circulated in the tunnel for the first time since the
 541 incident. This also marked the start of the main research programme and the beginning
 542 of the so-called Run 1: first operational run (2009 - 2013).

543 Performance of the LHC

544 In June 2015 the LHC restarted delivering physics data, after a two-year break, the so-
 545 called Long Shutdown 1 (LS1), during which the magnets were upgraded to handle the
 546 current required to circulate 7-TeV beams. It was the beginning of the so-called Run 2 -
 547 second operational run (2015-2018) - during which LHC has collided up to 10^{11} bunches
 548 of protons every 25 ns at the design luminosity - the highest luminosity the detector was
 549 designed to cope with - of $2 \cdot 10^{34} \text{ cm}^{-2} \text{s}^{-1}$. The definition of the luminosity is:

$$\mathcal{L} = f \frac{n_b N_1 N_2}{4\pi\sigma_x\sigma_y} \quad (2.1)$$

550 where N_1 and N_2 are the number of protons per bunch in each of the colliding beams, f
 551 is the revolution frequency of the bunch collisions, n_b the number of proton per bunch,
 552 and σ_x and σ_y are the horizontal and vertical dimensions of the beam. The luminosity is
 553 strictly related to the number of collisions occurring during a certain experiment via the
 554 following:

$$\mathcal{N}_{\text{event}} = \mathcal{L}\sigma_{\text{event}} \quad (2.2)$$

555 where σ_{event} is the cross section of the process under investigation. It has not only collided
 556 protons but also heavy ions, in particular lead nuclei at $\sqrt{s_{NN}} = 5.02 \text{ TeV}$, at a luminosity
 557 of $10^{27} \text{ cm}^{-2} \text{s}^{-1}$ [23].

558 Acceleration stages

559 Before reaching the maximum energy, the proton beams are accelerated by smaller ac-
 560 celerators through various stages. Figure 2.1 shows a sketch of the CERN's accelerator
 561 complex. It all begins at the linear accelerator LINAC 2. Here protons are accelerated up
 562 to 50 MeV, and then injected in the Proton Synchrotron Booster (PSB) where they reach

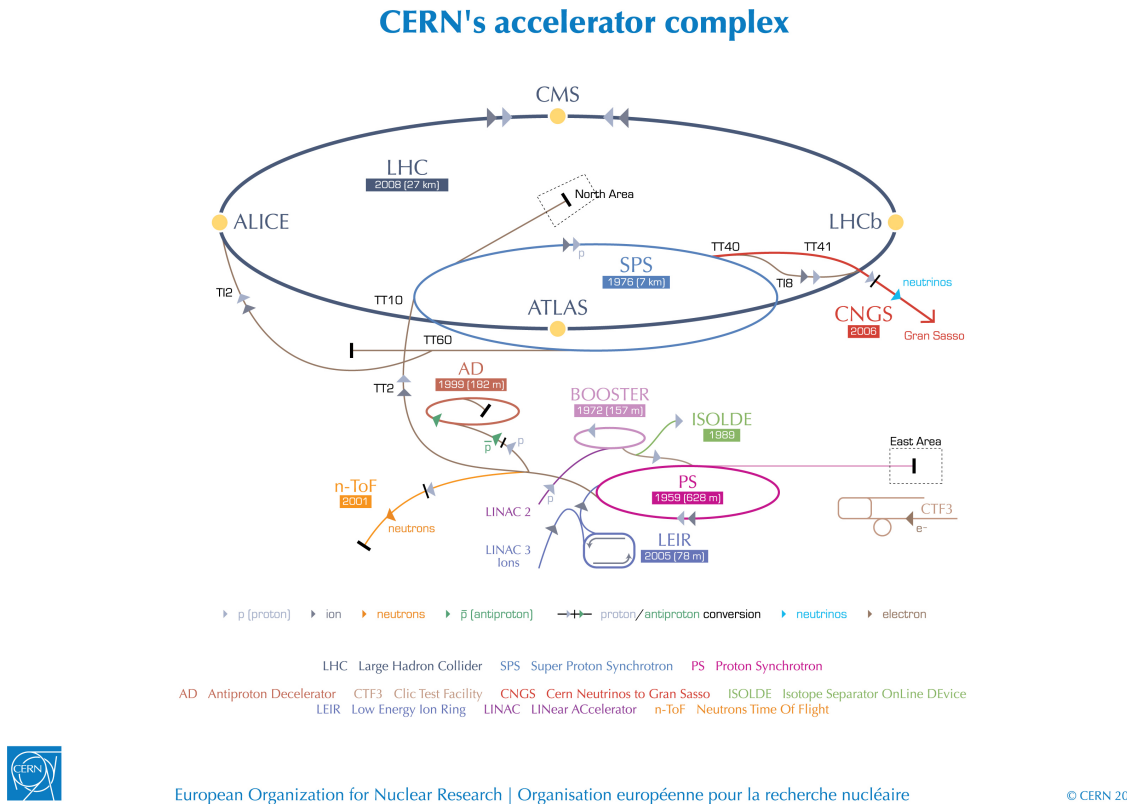


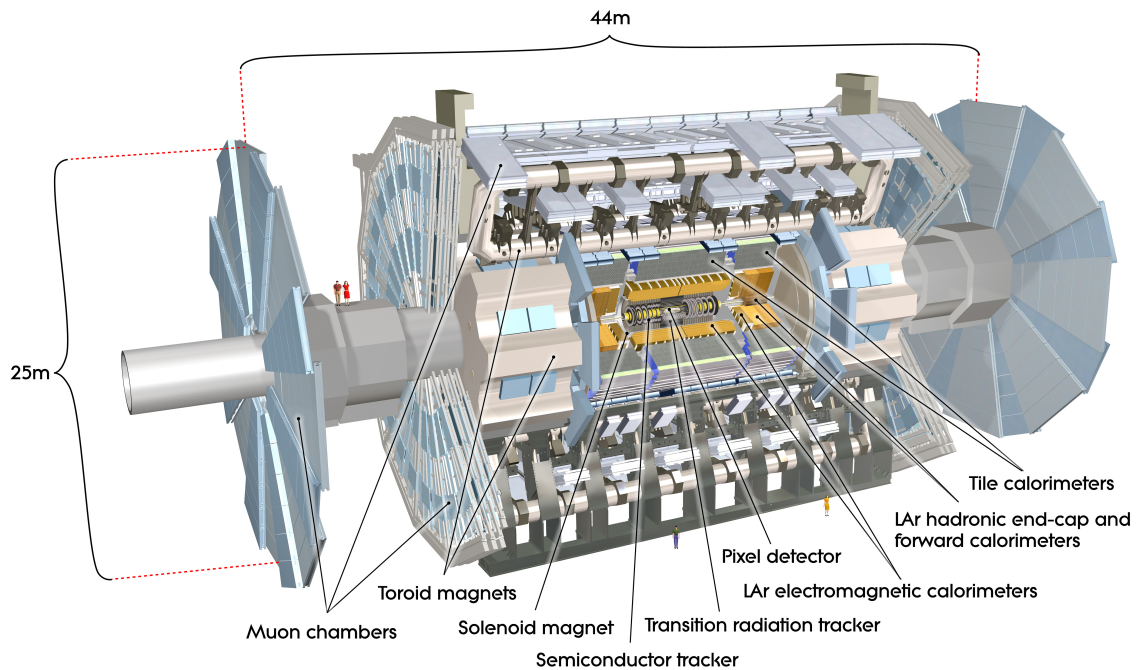
Figure 2.1: CERN Accelerator complex. The LHC is the last ring (dark grey line). Smaller machines are used for early-stage acceleration and also to provide beams for other experiments [3].

563 1.4 GeV. The next stage is the Proton Synchrotron (PS), which boosts the beams up to 25
564 GeV and then the Super Proton Synchrotron (SPS) makes them reach energies up to 450
565 GeV. Eventually, the beams are injected in bunches with a 25 ns spacing into the LHC,
566 where they travel in opposite directions, while they are accelerated to up to 13 TeV. Once
567 the bunches reach the maximum energy, they are made collide at four different points,
568 inside four experiments around the ring [24].

569 The heavy ion beams acceleration procedure is slightly different. Their journey starts
570 at LINAC 3 first, and the Low Energy Ion Ring (LEIR) then, before they make their way
571 into the PS where they follow the same path as the protons [24].

572 The four large detectors on the collision points are; the multi-purpose detectors A Tor-
573 oidal LHC ApparatuS (ATLAS), and Compact Muon Solenoid (CMS) [25], Large Hadron
574 Collider beauty (LHCb) [26], which focuses on flavour physics, and A Large Ion Collider
575 Experiment (ALICE) [27] which specialises in heavy ion physics. The *big four* are not the
576 only experiments at the CERN's accelerator complex. There also are smaller experiments
577 based at the the four caverns about the collision points e.g. TOTEM, LHCf and MoEDAL,
578 but this will not be discussed any further in this thesis.

579 2.2 The ATLAS Detector



580 Figure 2.2: Cut-away view of the ATLAS detector. The dimensions of the detector are 25 m in height and 44
581 m in length. The overall weight of the detector is approximately 7000 tonnes [3].

582 ATLAS is a general-purpose detector designed to collect data with the highest luminosity provided by the LHC. It is located at CERN’s Point 1 cavern and it measures about 583 45 m in length and 25 m in diameter. It has a forward-backward symmetric cylindrical 584 geometry with respect to the interaction point and it is designed to reconstruct and measure 585 physics objects such as electrons, muons, photons and hadronic jets. Its design was 586 optimised to be as sensitive as possible to the discovery of the Higgs boson and beyond-the-Standard-Model (BSM) physics. In fact, thanks to the other sub-systems, ATLAS is 587 able to observe all possible decay products by covering nearly 4π steradians of solid angle.

588 In Figure 2.2 a cut-away view of ATLAS with all its components is shown. The innermost 589 layer is the Inner Detector (ID) which is the core of the tracking system and consists 590 of a Pixel, a Silicon micro-strip tracker (SCT), and a Transition Radiation Tracker (TRT). 591 It is submerged in a 2 T magnetic field, generated by a thin superconducting solenoid, 592 which bends all the charged particles’ trajectories allowing transverse momentum measurement. The electromagnetic and hadronic calorimeters form the next layer and they are 593 both used to perform precise energy measurements of photons, electrons, and hadronic 594 jets. Finally, the outermost layer corresponds to the Muon Spectrometer (MS) which, to-

596 gether with the ID, enclosed in a toroidal magnetic field, allows precise measurement of
 597 momentum and position of muons. These sub-detectors will be discussed in more detail
 598 in the following sections.

599 The ATLAS coordinate system

600 A coordinate system is taken on for the spatial definition of the sub-systems and kinematic
 601 measurement of physics processes. Such system is defined starting from the interaction
 602 point, defined as the origin. The z -axis is defined by the beam direction and the $x - y$
 603 plan, as transverse to the beam direction.

604 A quantity, known as pseudorapidity, (η), is defined to describe the angle of a particle
 605 coming out of the collision, with respect to the beam axis:

$$\eta \equiv -\ln(\tan(\theta/2))$$

606 Here θ is the polar angle. The azimuthal angle, ϕ , is defined around the beam axis and
 607 the polar angle. In the (η, ϕ) space a distance ΔR can be therefore defined as

$$\Delta R = \sqrt{\Delta\eta^2 + \Delta\phi^2}$$

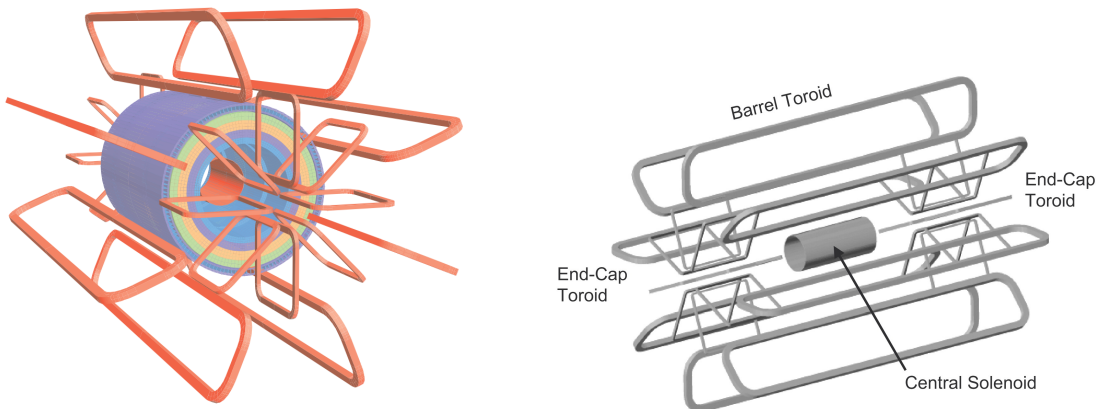
608 where $\Delta\eta$ and $\Delta\phi$ are the differences in pseudorapidity and azimuthal angle between any
 609 two considered objects. A central and a forward region of pseudorapidity are also defined
 610 such that the detector components are described as part of the *barrel* if they belong to the
 611 former or as part of the *end-caps* if they belong to the latter.

612 2.2.1 The Magnet System

613 The ATLAS magnet system, 26 m long with a 22 m diameter, generates the magnetic field
 614 needed to bend the trajectories of charged particles in order to perform momentum meas-
 615 urement. Figure 2.3a and 2.3b show the geometry of the system and its components,
 616 which are made of NbTi - superconducting material - and will be described in the follow-
 617 ing paragraphs.

618 The Central Solenoid

619 With an axial length of 5.8 m, an inner radius of 2.46 m, and an outer radius of 2.56 m, the
 620 central solenoid magnet is located between the ID and the ECAL. Its function is to bend
 621 the charged particles that go through the ID and it is aligned on the beam axis providing a
 622 2 T axial magnetic field that allows accurate momentum measurement up to 100 GeV [28].



(a) Geometry of magnet windings and tile calorimeter steel. The eight barrel toroid coils, with the end-cap coils interleaved are visible. The solenoid winding lies inside the calorimeter volume [4].

(b) Schematic view of the superconducting magnets [28].

Figure 2.3: The ATLAS magnet system.

623 The Barrel and the End-cap Toroids

624 Figure 2.3b displays the toroid magnetic system that surrounds the calorimeters. With its
 625 cylindrical shape this component consists of a barrel and two end-caps toroids, each with
 626 eight superconducting coils. The system allows accurate measurement of muon momenta
 627 using a magnetic field of approximately 0.5 T (barrel) for the central regions and 1 T (end-
 628 cap) for the end-cap regions, respectively, which bends the particles in the θ direction.

629 2.2.2 The Inner Detector

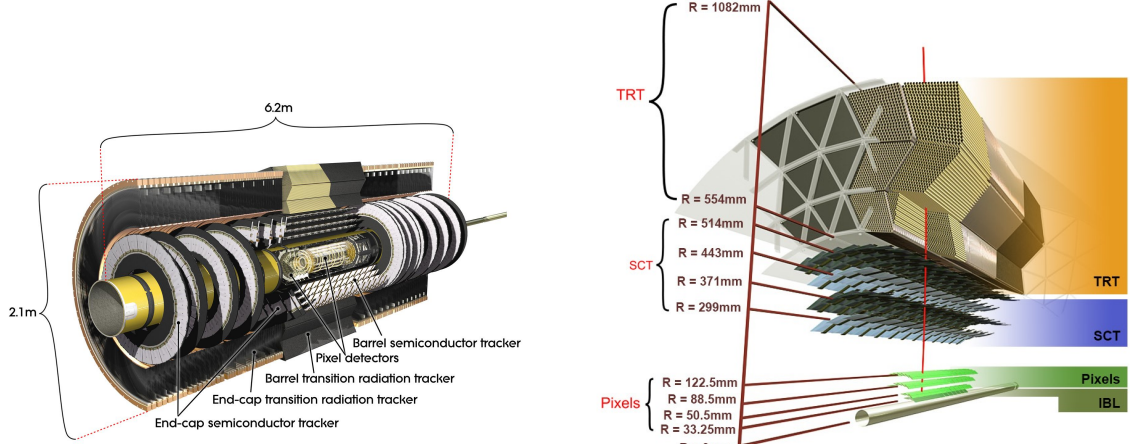
630 The Inner Detector (ID) [29] is the innermost component of the ATLAS detector i. e. the
 631 nearest sub-detector to the interaction region and it is used to reconstruct charged particle
 632 tracks used in the selection of physics objects. In fact, it allows robust track reconstruction,
 633 with accurate impact parameter resolution ($\sim 20\mu m$) and precise primary and secondary
 634 vertex reconstruction for charged particles (tracks) above 500 MeV and within $|\eta| < 2.5$.

635 The ID is comprised of independent and concentric sub-systems, which are all shown
 636 in Figure 2.4:

637 • Insertable B-Layer (IBL):

638 innermost Pixel Detector layer added during ATLAS Run 2 upgrade (2013/2014) to
 639 improve vertexing and impact parameter reconstruction;

640 • Silicon Pixel Tracker (Pixel):



(a) Overview of the ATLAS ID with labels and dimensions.

(b) Diagram of the ATLAS ID and its sub-detectors.

Figure 2.4: The ATLAS Inner Detector

made of silicon pixel layers and used mainly for reconstructing both the primary and secondary vertices in an event;

• SemiConductor Tracker (SCT):

comprised of silicon microstrip layers; thanks to its resolution ($17 \times 580 \mu\text{m}$) it can accurately measure particle momenta;

• Transition Radiation Tracker (TRT):

final layer comprised of various layers of gaseous straw tube elements surrounded by transition radiation material.

These sub-detectors will be discussed in the following sections.

IBL

The IBL [30] is the innermost Pixel Detector layer as shown in Figure 2.4b. It is comprised of 6M channels and each pixel measures $50 \times 250 \mu\text{m}$. Its resolution is $8 \times 40 \mu\text{m}$. The addition of this new layer brought a considerable improvement on the performance of the Pixel Detector by enhancing the quality of impact parameter reconstruction of tracks. In particular, this was achieved by improving the vertex finding efficiency and the tagging of bottom-quark-initiated jets (b -jets) which, in case of a B-layer failure, can be restored by the IBL. Besides these improvements, the IBL insertion allowed ATLAS to better cope with high luminosity effects such as the increase in event pile-up, which leads to high occupancy and read-out inefficiency.

660 Pixel

661 The Pixel detector is comprised of 1750 identical sensorchip-hybrid modules, each cover-
 662 ing an active area of 16.4×60.8 mm. The total number of modules correspond to roughly
 663 80 million semiconductor silicon pixels. The nominal pixel size is $50 \mu\text{m}$ in the ϕ direction
 664 and $400 \mu\text{m}$ in the barrel region, along the z -axis (beam axis) [31]. The reason why such a
 665 large amount of pixels is employed is justified by the need to cope with the high luminos-
 666 ity in ATLAS. The silicon pixel detector measures 48.4 cm in diameter and 6.2 m in length
 667 providing a pseudorapidity coverage of $|\eta| < 2.5$. Figure 2.4b shows the three concentric
 668 barrel layers placed at 50.5 mm, 88.5 mm and 122.5 mm respectively. Furthermore, the
 669 Pixel detector is made of six disk layers, three for each forward region, such that when a
 670 charged particle crosses the layers it will generate a signal at least in three space points.
 671 The fine granularity of such detector allows accurate measurement and precise vertex re-
 672 construction, as it provides a more accurate position measurement as a large detection
 673 area is available. In particular, it has a resolution of $10 \times 115 \mu\text{m}$.

674 SCT

675 The SCT is made of 4088 modules of silicon micro-strip detectors arranged in four con-
 676 centric barrel layers. It is mainly used for precise momentum reconstruction over a range
 677 $|\eta| < 2.5$ and it was designed for precision measurement of the position using four points
 678 (corresponding to eight silicon layers), obtained as track hits when crossing the layers.
 679 Figure 2.4b shows the structure of the SCT with its four concentric barrel layers with radii
 680 ranging from 299 mm to 514 mm and two end-cap layers. Each module has an intrinsic
 681 resolution of $17 \mu\text{m}$ in the $R - \phi$ direction and $580 \mu\text{m}$ in the z direction. As the SCT is fur-
 682 ther away from the beam-pipe than the Pixel detector, it has to cope with reduced particle
 683 density. This allows for reduced granularity maintaining the same level of performance of
 684 the Pixel detector: SCT can use ~ 6.3 million read-out channels.

685 TRT

686 The last and outermost of the sub-systems in the ID is the TRT. It is a gaseous detector
 687 which consists of 4 mm diameter straw tubes wound from a multilayer film reinforced
 688 with carbon fibers and containing a $30 \mu\text{m}$ gold plated tungsten wire in the center. The
 689 straw is filled with a gas mixture of 70% Xe, 27% CO₂ and 3% O₂ [32]. As shown in
 690 Figure 2.4b, its section consists of three concentric layers with radii ranging from 544 mm
 691 to 1082 mm, each of which has 32 modules containing approximately 50,000 straws, 1.44 m

in length, aligned parallel to the beam direction with independent read-out at both ends.
 Both end-cap sections are divided into 14 wheels, with roughly 320,000 straws in the R-direction. The average 36 hits per track in the central region of the TRT allow continuous tracking to enhance pattern recognition and momentum resolution in the $|\eta| < 2.5$ region.
 It also improves the p_T resolution for longer tracks.

2.2.3 The Calorimeters

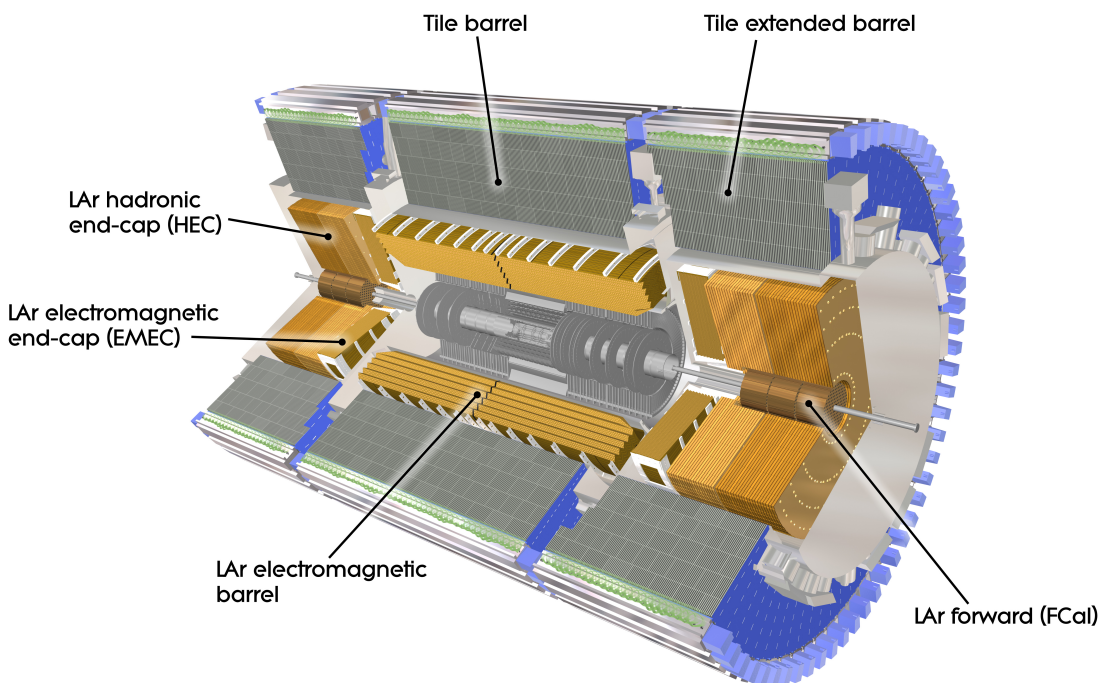


Figure 2.5: A computer generated image of the full calorimeter.

The ATLAS Calorimeter system, shown in Figure 2.5, is comprised of two main subsystems; the electromagnetic calorimeter (ECAL) and hadronic calorimeter (HCAL), which are designed to stop and measure the energy of electromagnetic-interacting and hadronic particles respectively. The combination of the two provides full coverage in ϕ and $|\eta| < 4.95$. Particles slow down and lose energy generating showers when crossing different layers. The ECAL is comprised of one barrel and two end-cap sectors employing liquid Argon (LAr). The showers hereby develop as electrons pairs which are then collected. The HCAL is also comprised of one barrel and two end-cap sectors. The sensors in the barrel of the HCAL are tiles of scintillating plastic whereas LAr is employed for the end-cap. A forward region, the closest possible to the beam, is covered by a LAr forward calorimeter (FCal). The LAr and Tile Calorimeter will be briefly discussed in the

709 following paragraphs.

710 The Liquid Argon Calorimeters

711 The ECAL is comprised of multiple layers of liquid Argon (LAr) sampler and lead ab-
712 sorber. The choice of its accordion-geometry design brought two main advantages; full
713 ϕ coverage with no non-interactive regions (no cracks); fast extraction of signals coming
714 from both front or rear end of the electrodes. It is made of two half-barrel wheels, both
715 placed in the barrel cryostat, that provide a pseudorapidity coverage up to $|\eta| < 1.475$
716 and two end-cap detectors providing $1.375 \leq |\eta| \leq 3.20$ coverage in two end-cap cryo-
717 stats. The junction between the barrel and end cap components defines the crack region
718 and any signal coming from the crack region is therefore discarded.

719 In the $|\eta| < 1.8$ region there is an additional layer, placed at the front of the calorimeter,
720 that is made of a thin (0.5 cm in the end-cap and 1.1 cm in the barrel) LAr layer with
721 no absorber [33]. This additional layer was designed to correct for the energy lost, as
722 particles enter the calorimeter, by taking a measurement just before the majority of the
723 electromagnetic shower is developed.

724 The Tile calorimeter

725 The main purpose of the hadronic calorimeter is to measure the energy of hadronic showers.
726 It is built employing steel and scintillating tiles coupled to optical fibres which are read
727 out by photo-multipliers. As shown in Figure 2.5, the HCAL is made up of three cylin-
728 ders; a central barrel, 5.64 m long covering a region $|\eta| < 1.0$, and two extended barrel,
729 2.91 m long covering a reigon $0.8 < |\eta| < 1.7$. Each cylinder is made up of 64 modules
730 and each module is in turn made up of three layers. Ultimately, the smallest section of the
731 calorimeter module is a cell with a $\Delta\phi \times \Delta\eta = 0.1 \times 0.1$ granularity for the two innermost
732 layers and $\Delta\phi \times \Delta\eta = 0.2 \times 0.1$ for the outermost one.

733 2.2.4 The Muon Spectrometer

734 The MS [34], shown in Figure 2.6, is the outermost sub-system of the whole ATLAS de-
735 tector. As such, it surrounds the calorimeters and its main function is to perform precision
736 measurement of muons momenta. The deflection of muon tracks employing large super-
737 conducting air-core toroid magnets and high-precision tracking chambers is at the heart
738 of such high precision measurement.

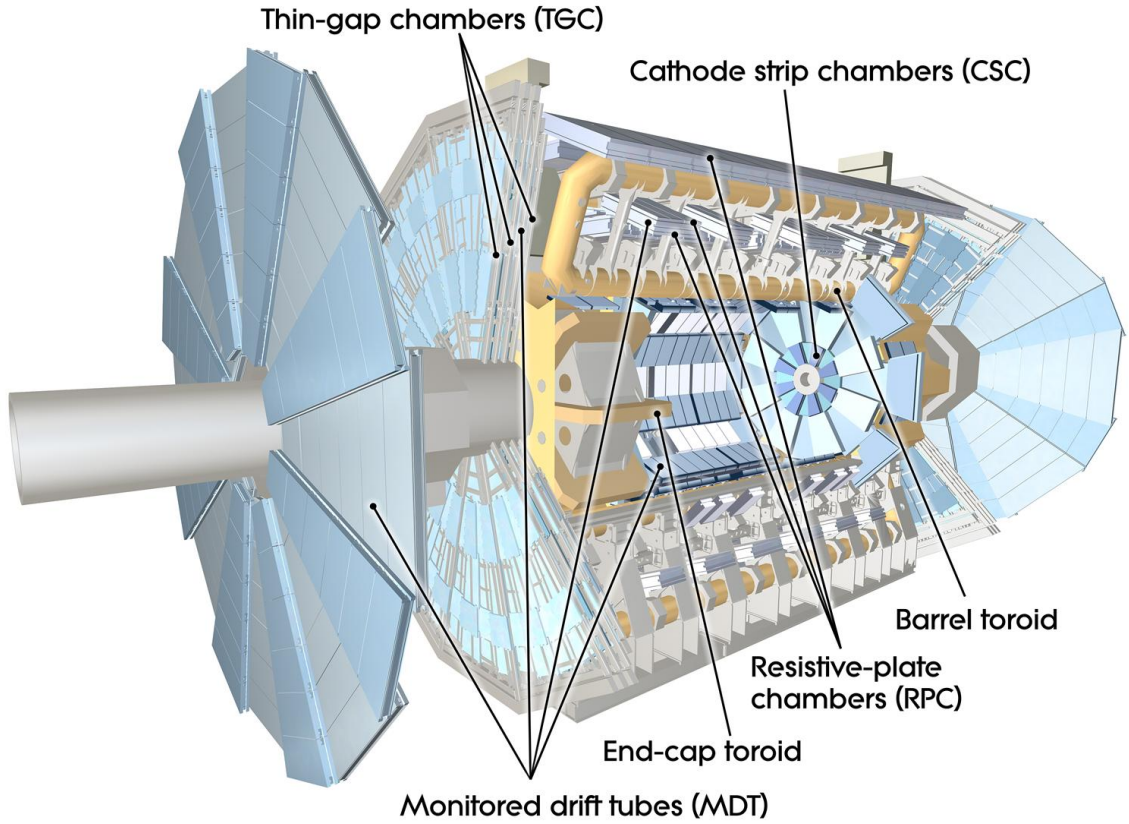


Figure 2.6: Cut-away view of the ATLAS muon system [4].

739 The MS is comprised of one large barrel toroid, covering the region $|\eta| \leq 1.4$, and
 740 two end-cap toroids, covering $1.6 < |\eta| \leq 2.7$ which are employed together to achieve the
 741 track-bending effect wanted. The magnitude of the magnetic field in the barrel, generated
 742 by eight large superconducting coils, ranges from 0.5 to 2 T.

743 Around the beam axis, three cylindrical layers make way for the chambers, placed in
 744 planes perpendicular to the beam, used to measure tracks.

745 Monitored Drift Chambers (MDTs) are employed over most of the pseudorapidity
 746 range to provide precision measurement of track coordinates in the bending direction.
 747 Cathode Strip Chambers (CSCs) are instead employed at large pseudorapidity ($2 < |\eta| <$
 748 2.7). Finally, in the end-cap regions Thin-Gap Chambers (TGCs) together with Resistive-
 749 Plate Chambers (RPCs) are dedicated to the Trigger System discussed in Section 2.3.

750 2.3 The ATLAS Trigger System

751 The ATLAS Trigger System is at the heart of data taking. It is an essential component of
 752 any nuclear or particle physics experiment since it is responsible for deciding whether or
 753 not to store an event for later study [5]. The ATLAS Trigger system is employed to reduce

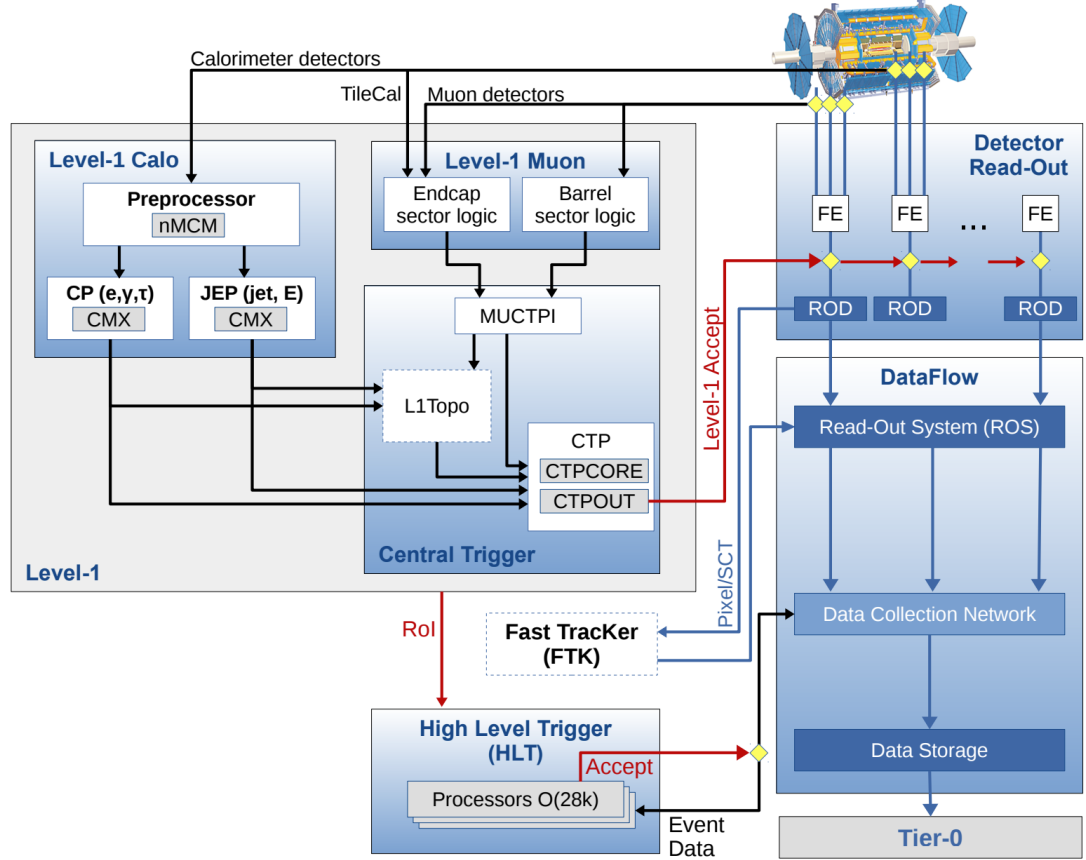


Figure 2.7: The ATLAS TDAQ system. L1Topo and FTK were being commissioned during 2015 and not used for the results shown in this thesis [5].

754 the event rate from $\sim 40 \text{ MHz}$ ¹ bunch-crossing² to $\sim 200 \text{ Hz}$ which corresponds to roughly
 755 300 MB/s .

756 The Trigger and Data Acquisition (TDAQ) system shown in Figure 2.7 consists of a
 757 hardware-based first level trigger (L1) and a software-based high-level trigger (HLT). The
 758 L1 trigger decision is formed by the Central Trigger Processor (CTP), which receives in-
 759 puts from the L1 calorimeter (L1Calo) and L1 muon (L1Muon) triggers. The first level
 760 (L1), which was designed to perform the first selection step, is a hardware-based system
 761 that uses information from the calorimeter and muon subdetectors. It also defines the
 762 so-called Regions of Interest (RoIs) within the detector to be investigated by the next level
 763 trigger, the HLT. Additionally, a Fast TracKer (FTK) system [35] (not yet installed) will
 764 provide global ID track reconstruction at the L1 trigger rate using lookup tables stored in

¹ The LHC delivers beams with a bunch-spacing of 25 ns.

² The term bunch-crossing is hereby used when referring to a collision between two bunches of protons. Since only a certain fraction of the total momentum carried by each proton contributes to the collision, an average number of interactions per bunch-crossing, $\langle \mu \rangle$ is used.

⁷⁶⁵ custom associative memory chips for the pattern recognition. The FPGA-based track fitter
⁷⁶⁶ will perform a fast linear fit and the tracks are made available to the HLT. This system will
⁷⁶⁷ allow the use of tracks at much higher event rates in the HLT than is currently affordable
⁷⁶⁸ using CPU systems. However, the upgrade of the ATLAS trigger will not be discussed
⁷⁶⁹ any further.

⁷⁷⁰ In the next sections the L1 and HLT will be briefly described.

⁷⁷¹ 2.3.1 Level 1 Trigger

⁷⁷² The Level 1 Trigger identifies Regions of Interest (RoIs)³ and passes these to HLT which
⁷⁷³ will perform further investigations. Furthermore, in order to decide whether or not the
⁷⁷⁴ event processing will continue, L1 selection uses only information coming from some
⁷⁷⁵ parts of the detector to keep the input rate to a maximum of 100 kHz. L1 is implemented
⁷⁷⁶ in fast custom electronics to keep the latency⁴ below 2.5 μ s. Event data from other sub-
⁷⁷⁷ syststem are temporarily stored in memories whilst L1 decision is taken.

⁷⁷⁸ The L1 topological trigger (L1-Topo) [36] is feeded with energy and direction inform-
⁷⁷⁹ ation, about the objects found by the L1 calorimeter and the muon trigger, which will be
⁷⁸⁰ processed by dedicated algorithms implemented in its own FPGAs. However, due to the
⁷⁸¹ 100 kHz read-out rate, not all the information collected by L1-Topo will be sent to the HLT,
⁷⁸² but only part of it. In order to properly seed the ROI-guided HLT reconstruction, specific
⁷⁸³ objects in combination with the correct topological criteria must be employed.

⁷⁸⁴ 2.3.2 High-Level Trigger

⁷⁸⁵ The HLT is used to reduce the output rate down to 1 kHz and it has a \sim 200 ms average
⁷⁸⁶ decision time. Events that pass L1 trigger are then processed by the HLT using finer-
⁷⁸⁷ granularity calorimeter information, precision measurements from the MS and tracking
⁷⁸⁸ information from the ID. The HLT reconstruction can be run within RoIs identified at L1
⁷⁸⁹ or a so-called full-scan on the full detector can be performed. The track reconstruction in
⁷⁹⁰ the Inner Detector is an essential component of the trigger decision in the HLT and it will
⁷⁹¹ be discussed more in detail in Chapter 3

³ $\eta - \phi$ regions where event features have been found by the L1 selection process.

⁴ Time needed by an electric signal to get to the front-end electronics.

3

The ATLAS Trigger System

792 The ATLAS trigger system together with its performance will be presented in the follow-
 793 ing chapter. A brief introduction, about the reason behind the need of a trigger system to-
 794 gether with its implementation in ATLAS will be discussed in Section 3.1. The algorithms
 795 used for the tracking in the inner detector will then be described in Section 3.2. Ultimately,
 796 measurements of the performance of the low transverse momentum single lepton triggers
 797 and medium and high transverse momentum b -jet triggers, as part of the *qualification task*¹
 798 of the author, will be discussed in Section 3.3.
 799

800 3.1 What is the Trigger needed for?

801 In 2016 and 2017 LHC performed incredibly well delivering $\sim 80\text{fb}^{-1}$ of pp collisions.
 802 As previously mentioned in Section 2.3, due to storage space limitations it is not feasible
 803 to save all the information about the collision after every bunch crossing, so the ATLAS
 804 Trigger System is indispensable to reduce the read-out rate to a sensible value without af-
 805 fecting the physics programme of ATLAS e. g. discarding potentially interesting events. A
 806 multiple-level architecture is employed to allow the trigger some more time such that the
 807 identification, of an interesting event using both software- and hardware-based real-time
 808 algorithms to determine whether or not a bunch-crossing contains interesting physics, is
 809 made possible.

810 The two levels

¹ In order to become an ATLAS author, a person must have been an active ATLAS member for at least one year doing ATLAS technical work

811 3.2 The tracking**812 3.3 Performance of HLT****813 3.3.1 Electrons****814 3.3.2 Muons****815 3.3.3 b -jets**

816 **4** | Event Simulation and Reconstruction

817

818 bla bla bla

819 **4.1 Event Simulation**

820 bla bla

821 bla bla

822 bla bla

823 bla bla

824 **4.1.1 Event Generation**

825 bla bla bla

826 bla bla bla

827 bla bla bla

828 bla bla bla

829 **4.1.2 Detector Simulation**

830 bla bla bla

831 bla bla bla

832 bla bla bla

833 **4.2 Object Reconstruction**

834 bla bla bla

835 bla bla bla

836 4.2.1 Tracks and vertices

837 bla bla bla

838 bla bla bla

839 4.2.2 Electrons

840 bla bla bla

841 bla bla bla

842 4.2.3 Muons

843 bla bla bla

844 bla bla bla

845 4.2.4 Jets

846 bla bla bla

847 bla bla bla

848 4.2.5 Missing Transverse Energy

849 bla bla bla

850 bla bla bla

851 4.2.6 Overlap Removal

852 bla bla bla

853 bla bla bla

854 **5**

| Stop searches in final states with
855 jets and missing transverse en-
856 ergy

857 **6** | Results and Statistical Interpretations

858

⁸⁵⁹ **Appendix A**

Bibliography

- [1] ATLAS Collaboration, "Summary plots from the atlas standard model physics group." https://atlas.web.cern.ch/Atlas/GROUPS/PHYSICS/CombinedSummaryPlots/SM/ATLAS_a_SMSummary_TotalXsect/ATLAS_a_SMSummary_TotalXsect.png. viii, 9
- [2] C. Borschensky, M. Krämer, A. Kulesza, M. Mangano, S. Padhi, T. Plehn, and X. Portell, *Squark and gluino production cross sections in pp collisions at $\sqrt{s} = 13, 14, 33$ and 100 TeV*, *Eur. Phys. J.* **C74** no. 12, (2014) 3174, [arXiv:1407.5066 \[hep-ph\]](https://arxiv.org/abs/1407.5066). viii, 18
- [3] C. Lefèvre, *The CERN accelerator complex*, <http://cds.cern.ch/record/1260465>. ix, 22, 23
- [4] ATLAS Collaboration, *The ATLAS experiment at the CERN Large Hadron Collider*, *Journal of Instrumentation* **3** no. 08, (2008) S08003. <http://stacks.iop.org/1748-0221/3/i=08/a=S08003>. ix, 25, 30
- [5] A. Collaboration, *Performance of the ATLAS Trigger System in 2015*, *Eur. Phys. J.* **C77** (2017), [arXiv:1611.09661 \[hep-ex\]](https://arxiv.org/abs/1611.09661). ix, 30, 31
- [6] M. Herrero, *The Standard Model*, <https://arxiv.org/abs/hep-ph/9812242>. 3
- [7] ATLAS Collaboration, *Observation of a New Particle in the Search for the Standard Model Higgs Boson with the ATLAS Detector at the LHC*, *Phys.Lett.* **B716** (2012), [arXiv:1207.7214 \[hep-ex\]](https://arxiv.org/abs/1207.7214). 3
- [8] CMS Collaboration, *Observation of a new boson at a mass of 125 GeV with the CMS experiment at the LHC*, *Phys.Lett.* **B716** (2012), [arXiv:1207.7235 \[hep-ex\]](https://arxiv.org/abs/1207.7235). 3
- [9] A. Pich, *The Standard Model of Electroweak Interactions*, [arXiv:1201.0537 \[hep-ph\]](https://arxiv.org/abs/1201.0537). 6, 7

- 884 [10] K. A. Olive at al. (Particle Data Group), *Review of Particle Physics*, *Chin.Phys. C* **38**(9)
 885 (2014). 6
- 886 [11] J. Goldstone, A. Salam and S. Weinberg, *Broken Symmetries*, *Phys. Rev.* **127** (1962)
 887 965–970. 8
- 888 [12] S. Weinberg, *Implications of Dynamical Symmetry Breaking*, *Phys. Rev.* **D19** (1976)
 889 1277–1280. 10
- 890 [13] Super-Kamiokande Collaboration, Y. Fukuda et al., *Evidence for oscillation of*
 891 *atmospheric neutrinos*, *Phys. Rev. Lett.* **81** (1998) 1562–1567, [arXiv:hep-ex/9807003](https://arxiv.org/abs/hep-ex/9807003)
 892 [[hep-ex](#)]. 10
- 893 [14] SNO Collaboration, *Measurement of the Rate of $\nu_e + d \rightarrow p + p + e^-$ Interactions*
 894 *Produced by 8B Solar Neutrinos at the Sudbury Neutrino Observatory*, *Phys. Rev. Lett.*
 895 **87** (2001). 10
- 896 [15] T. O. W. of the Nobel Prize.
 897 https://www.nobelprize.org/nobel_prizes/physics/laureates/2015/. 10
- 898 [16] F. Jegerlehner, *The hierarchy problem of the electroweak Standard Model revisited*,
 899 [arXiv:1305.6652](https://arxiv.org/abs/1305.6652) [[hep-ph](#)]. 12
- 900 [17] A. H. Chamseddine, R. Arnowitt, and P. Nath, *Locally Supersymmetric Grand*
 901 *Unification*, *Phys. Rev. Lett.* **49** (1982) 970–974.
 902 <https://link.aps.org/doi/10.1103/PhysRevLett.49.970>. 13
- 903 [18] A. Arbey, M. Battaglia, A. Djouadi, F. Mahmoudi, and J. Quevillon, *Implications of a*
 904 *125 GeV Higgs for supersymmetric models*, *Physics Letters B* **708** no. 1, (2012) 162 – 169.
 905 <http://www.sciencedirect.com/science/article/pii/S0370269312000810>. 13
- 906 [19] L. Randall and R. Sundrum, *Out of this world supersymmetry breaking*, *Nucl. Phys.*
 907 **B557** (1999) 79–118, [arXiv:hep-th/9810155](https://arxiv.org/abs/hep-th/9810155) [[hep-th](#)]. 13
- 908 [20] G. F. Giudice, M. A. Luty, H. Murayama, and R. Rattazzi, *Gaugino mass without*
 909 *singlets*, *JHEP* **12** (1998) 027, [arXiv:hep-ph/9810442](https://arxiv.org/abs/hep-ph/9810442) [[hep-ph](#)]. 13
- 910 [21] H. E. Haber and G. L. Kane, *The Search for Supersymmetry: Probing Physics Beyond the*
 911 *Standard Model*, *Phys. Rept.* **117** (1985) 75–263. 14
- 912 [22] K. Hidaka and A. Bartl, *Impact of bosonic decays on the search for the lighter stop and*
 913 *sbottom squarks*, *Phys. Lett.* **B501** (2001) 78–85, [arXiv:hep-ph/0012021](https://arxiv.org/abs/hep-ph/0012021) [[hep-ph](#)]. 14

- 914 [23] J.M. Jowett, M. Schaumann, R. Alemany, R. Bruce, M. Giovannozzi, P. Hermes, W.
 915 Hofle, M. Lamont, T. Mertens, S. Redaelli, J. Uythoven, J. Wenninger, *The 2015*
 916 *Heavy-Ion Run of the LHC*,
 917 <http://accelconf.web.cern.ch/accelconf/ipac2016/papers/tupmw027.pdf>. 21
- 918 [24] O. S. Brüuning, P. Collier, P. Lebrun, S. Myers, R. Ostojic, J. Poole and P. Proudlock,
 919 *LHC Design Report*, <https://cds.cern.ch/record/782076>. 22
- 920 [25] CMS Collaboration, *The CMS experiment at the CERN LHC*, Journal of
 921 Instrumentation **3** no. 08, (2008) S08004.
 922 <http://stacks.iop.org/1748-0221/3/i=08/a=S08004>. 22
- 923 [26] LHCb Collaboration, et. al, *The LHCb Detector at the LHC*, **JINST** (2008). 22
- 924 [27] ALICE Collaboration, *The ALICE experiment at the CERN LHC*, Journal of
 925 Instrumentation **3** no. 08, (2008) S08002.
 926 <http://stacks.iop.org/1748-0221/3/i=08/a=S08002>. 22
- 927 [28] A. Yamamoto, Y. Makida, R. Ruber, Y. Doi, T. Haruyama, F. Haug, H. ten Kate,
 928 M. Kawai, T. Kondo, Y. Kondo, J. Metselaar, S. Mizumaki, G. Olesen, O. Pavlov,
 929 S. Ravat, E. Sbrissa, K. Tanaka, T. Taylor, and H. Yamaoka, *The ATLAS central*
 930 *solenoid*, **Nuclear Instruments and Methods in Physics Research Section A:**
 931 *Accelerators, Spectrometers, Detectors and Associated Equipment* **584** no. 1, (2008)
 932 **53 – 74**.
 933 <http://www.sciencedirect.com/science/article/pii/S0168900207020414>. 24,
 934 25
- 935 [29] ATLAS Collaboration, *The ATLAS Inner Detector commissioning and calibration*, **Eur.**
 936 **Phys. JC70** , [arXiv:1004.5293](https://arxiv.org/abs/1004.5293). 25
- 937 [30] ATLAS Collaboration, *ATLAS Insertable B-Layer Technical Design Report*,
 938 <https://cds.cern.ch/record/1291633>. 26
- 939 [31] G. A. et al., *ATLAS pixel detector electronics and sensors*, Journal of Instrumentation **3**
 940 no. 07, (2008) P07007. <http://stacks.iop.org/1748-0221/3/i=07/a=P07007>. 27
- 941 [32] A. Bingül, *The ATLAS TRT and its Performance at LHC*, Journal of Physics:
 942 Conference Series **347** no. 1, (2012) 012025.
 943 <http://iopscience.iop.org/article/10.1088/1742-6596/347/1/012025/meta>.
 944 27

-
- 945 [33] ATLAS Collaboration, *ATLAS liquid-argon calorimeter: Technical Design Report.*,
946 <https://cds.cern.ch/record/331061>. 29
- 947 [34] ATLAS Collaboration, *ATLAS muon spectrometer: Technical design report.*,
948 <https://cds.cern.ch/record/331068>. 29
- 949 [35] ATLAS Collaboration, *Fast TracKer (FTK) Technical Design Report.*,
950 <https://cds.cern.ch/record/1552953>. 31
- 951 [36] E. Simoni, *The Topological Processor for the future ATLAS Level-1 Trigger: from design to*
952 *commissioning*, [arXiv:1406.4316](https://arxiv.org/abs/1406.4316). 32